A role of oligodendrocytes in information processing independent of conduction velocity

Sharlen Moore[1,2,3,◊], Martin Meschkat[1,4], Torben Ruhwedel[1], Iva D. Tzvetanova[1], Andrea Trevisiol[1], Arne Battefeld[5,‡], Kathrin Kusch[1], Maarten Kole[5,6], Nicola Strenzke[7], Wiebke Möbius[1,4], Livia de Hoz[1,#,*], Klaus-Armin Nave[1]

[1]Department of Neurogenetics, Max Planck Institute of Experimental Medicine, Göttingen, Germany. [2]International Max Planck Research School for Neurosciences, Göttingen, Germany. [3]Göttingen Graduate School of Neurosciences and Molecular Biosciences, Germany. [4]Center for Nanoscale Microscopy and Molecular Physiology of the Brain, Göttingen, Germany. [5]Netherlands Institute for Neurosciences, Royal Netherlands Academy of Arts and Science, Amsterdam, The Netherlands. [6]Cell Biology, Faculty of Science, University of Utrecht, The Netherlands. [7]Institute for Auditory Neuroscience, University Medical Center, Göttingen, Germany.
[◊]Current address: Instituto de Fisiología Celular - Neurociencias, Universidad Nacional Autónoma de México, Mexico City, Mexico.
[#]Current address: Charité Medical University, Neuroscience Research Center, Berlin, Germany.
[‡]Current address: Institut des Maladies Neurodégénératives, Université de Bordeaux, Bordeaux, France.
[*]Corresponding author: dehoz@em.mpg.de

40   **Abstract**

41

42   Myelinating oligodendrocytes enable fast impulse propagation along axons as revealed

43   through studies of homogeneously myelinated white matter tracts. However, gray matter

44   myelination patterns are different, with sparsely myelinated sections leaving large

45   portions of the axons naked. The consequences of this patchy myelination for

46   oligodendrocyte function are not understood but suggest other roles in information

47   processing beyond the regulation of axonal conduction velocity. Here, we analyzed the

48   contribution of myelin to auditory information processing using paradigms that are good

49   predictors of speech understanding in humans. We compared mice with different degrees

50   of dysmyelination using acute cortical multiunit recordings in combination with behavioral

51   readouts. We identified complex alterations of neuronal responses that reflect fatigue and

52   temporal acuity deficits. Partially discriminable but overall similar deficits were observed

53   in mice with oligodendrocytes that can myelinate but cannot fully support axons

54   metabolically. Thus, myelination contributes to sustained stimulus perception in

55   temporally complex paradigms, revealing a role of oligodendrocytes in the CNS beyond

56   the increase of axonal conduction velocity.

Introduction

In the central nervous system (CNS), oligodendrocytes generate myelin, a multilayered sheath of membrane, spirally wrapped around axonal segments and best known for its role in enabling fast saltatory impulse propagation [1]. An additional function of oligodendrocytes is the metabolic support of myelinated axons [2–4], most important when axons spike at higher frequency [5]. Mouse mutants with abnormalities of CNS myelination have been used as models of human leukodystrophies and demyelinating diseases. However, analyses of these mice have been largely restricted to the diagnosis and assessment of severely reduced motor functions.

Importantly, at the network level, the contribution of CNS myelination to information processing remains poorly understood, in part because suitable phenotyping instruments have been lacking. Yet, there is an increasing awareness that myelination is required for higher-order brain functions. Subtle defects of the white matter have been associated with various psychiatric diseases [6]. Moreover, in the aging brain, the physiological decline of function is associated with subtle but widespread structural deterioration of myelin [7,8]. Functional studies of myelin have largely been restricted to motor behavior, which is under control of myelinated axons in white matter tracts, and to the fast impulse propagation and millisecond precision required for sound location in a highly specialized circuit of the brain stem [9]. However, myelin is also present within the cortical grey matter, where it is heterogeneous and patchy along projection neurons [10,11]. Moreover, a large fraction of the parvalbumin-positive interneuron axons are myelinated [12–14], even though their typical short distance to their target cells has been estimated to cause insignificant conduction delay times [13]. Oligodendrocyte lineage cells can myelinate axons in an activity dependent manner and influence their conduction velocity properties [15–19]. Mature oligodendrocytes respond to glutamatergic signals with enhanced glycolytic support of the axonal energy metabolism [4,5]. These data are compatible with the idea that myelin function in the CNS that go beyond regulating conduction velocity.

Indeed, there is still a major conceptual gap between the role of myelin in saltatory impulse propagation and its function at the network level. Virtually nothing is known about

88   the contribution of myelination to information processing, a function that should be most

89   evident for pathways that build on constant information transfer, as it is the case for the

90   auditory system. In the sound location system, nerve conduction velocity is fine-tuned by

91   myelination beginning at the brainstem level in order to facilitate sound localization [20,21].

92   However, the sound location system is a highly specialized circuit dedicated to sub-

93   millisecond precision of coincidence detection. Auditory processing is clearly broader than

94   sound localization and must constantly cope with the appearance of both short and

95   repetitive stimuli. This is essential e.g. for speech perception.

96

97   In humans, myelin abnormalities and nerve conduction velocities have been mostly

98   studied in terms of developmental delays, and rarely with respect to signal detection,

99   precision and acuity. And yet, it is clinically well known that patients with myelin disease,

100   similar to individuals at old age, show deficits in auditory processing [22,23] that cannot

101   simply be explained by delays in conduction velocity. For example, deficits in speech

102   recognition in noisy environments increase despite normal hearing thresholds [24], which

103   is suggestive of problems in temporal acuity, rather than the speed of processing.

104   In animal models of CNS dysmyelination, a few studies reported general auditory

105   abnormalities [25–28] or a specific delay at central auditory stations [29–31], as detected by

106   evoked response latencies. Using brainstem slices, e.g. Kim et al. reported excitability

107   defects at the Calyx of Held, a specialized synapse in the brainstem, important for sound

108   localization [28]. However, the perceptual consequences have not and cannot be assessed

109   with an *in vitro* system.

110

111   Here, we used a novel approach for the *in vivo* analysis of information processing and

112   perception in mice as a function of oligodendrocyte and myelin abnormalities. To

113   determine how dysmyelination and impairments in axonal metabolic support affect

114   temporal and spectral auditory processing, we compared adult wild type animals with

115   three lines of mutant mice. We used 1) the *shiverer* mice ($Mbp^{shi/shi}$) [32] as a model of

116   severe dysmyelination, 2) a newly generated *Mbp* allele ($Mbp^{neo/neo}$) as a hypomyelination

117   model (see below), and 3) mice with the heterozygous null allele of the *Slc16A1* gene

118   ($MCT1^{+/-}$) [3], encoding a monocarboxylate transporter (MCT1) that is required for

119   metabolic support. The use of these mouse models allowed the comparison of different

120   degrees of myelination, and to distinguish that from the role of oligodendrocytes in axonal

121   metabolic support.

122

123   Multiunit recordings of the cortex enabled us to test stimulus detection during auditory

124   processing in combination with behavioral readouts. Altered neuronal responses in the

125   auditory cortex of dysmyelinated mice were surprisingly complex, and included neuronal

126   fatigue, likely energy-related, and temporal acuity deficits that clearly exceeded the effect

127   of delays in conduction velocity. Moreover, deficits in "sound gap detection", a measure

128   relevant to speech recognition in humans, indicate that myelination of CNS axons is

129   critical for normal sound processing beyond the (data not shown) finely tuned conduction

130   velocity for sound localization. Our data reveal that CNS myelination not only speeds

131   impulse conduction but also determines the quality of information processing, which we

132   suggest is partially dependent on the metabolic roles of oligodendrocytes.

Results

To monitor auditory processing in the adult brain with compromised oligodendrocyte functions, we chose three types of mutant mice. To study the role of compacted myelin, we compared different *Mbp* mutations in mice. MBP is an abundant structural protein required for myelin growth and compaction [33,34]. One mutant is defined by the nearly complete absence of CNS myelin, the well-known *shiverer* (*Mbp^shi/shi^*) mouse [35] with a truncated *Mbp* gene [32]. The second *Mbp* model was newly generated for this study as a hypomorph mouse (*Mbp^neo/neo^*) with MBP expression levels below 50% as detailed below. A third mutant, heterozygous null for the *Slc16A1* gene (MCT1^+/-^) shows reduced expression of the monocarboxylate transporter MCT1, which is required by oligodendrocytes to metabolically support axons [3]. MCT1 enables the export of lactate and pyruvate and supports the generation of ATP in myelinated axons [5].

Mbp^neo^: a novel mouse mutant with reduced myelin sheath thickness

Shiverer mice have no compact myelin and a shivering phenotype that makes them suboptimal for behavioral testing. Since heterozygous *Mbp^shi/+^* mice show close to normal amounts of myelin [36], we sought to establish a hypomyelinated mouse model by reducing *Mbp* expression levels below 50% (see methods and Figure S1A), in agreement with earlier observations of transgenic complementation of *shiverer* mice [37,38]. Oligodendrocytes in adult *Mbp^neo/neo^* brains expressed 30% of the *Mbp* mRNA and 20% MBP at the protein level (Figures S1B and S1C). These mutants appeared clinically normal and were long-lived. Different from conventional *shivere*r mice, in which the vast majority of optic nerve axons are unmyelinated [35], *Mbp^neo/neo^* mice have 75% of their optic nerve axons myelinated (wild type: 92%). Importantly, this myelin was fully compacted but significantly thinner, as determined by g-ratio analysis (Figures S1D to S1F). Axon caliber distribution was not different between wild type and *Mbp^neo/neo^* mice (Figure S1G).

Central dysmyelination causes signs of auditory neuropathy

In wild type mice, all auditory projections, including the auditory nerve, are well myelinated [39,40]. Before studying the effect of dysmyelination on information processing, we determined latencies and amplitudes of sound-evoked responses at different auditory

164 stations using auditory brainstem responses (ABR), recorded *in vivo* through electrodes
165 located on the scalp (Figure 1A i). ABRs consisted of five waves (I-V) that reflect the
166 consecutive activation of the auditory nerve, cochlear nucleus, superior olive, lateral
167 lemniscus and inferior colliculus (Figure 1A ii). In the *Mbp*$^{shi/shi}$ mice, ABR waves were
168 significantly delayed at all auditory stations (Figures 1B and 1C) and delays increased
169 progressively. The peak-to-peak amplitude, which reflects the synchronous spiking in
170 response to sound onset, was unchanged in wave I (Figure 1F). This, together with the
171 findings that also response thresholds were not different from controls (Figures S2A and
172 S2B), confirms that cochlear function and peripheral conduction is normal in *Mbp*$^{shi/shi}$
173 mice. This was expected because the outer region of the auditory nerve is myelinated by
174 Schwann cells that do not require MBP for myelination (Figure 1A iii) [40]. However, the
175 amplitudes of waves II and III were reduced, and those of waves IV and V were increased
176 (Figures 1B and 1F). Such downstream improvements of diminished brainstem ABR
177 amplitudes have been observed in several animal models of auditory
178 synaptopathy/neuropathy (disorders of the inner hair cell ribbon synapse and/or auditory
179 nerve), and are thought to reflect compensatory mechanism of changes in gain to
180 peripheral hearing loss [41–46]. Hypomyelinated *Mbp*$^{neo/neo}$ mice were similarly normal with
181 respect to the shape of ABR wave I (Figures 1D and 1E) and threshold (Figure S2C).
182 They also showed a reduction in the amplitudes of waves II and III, and a larger wave V
183 at the IC level (Figure 1G). The *Mbp*$^{shi/shi}$ and *Mbp*$^{neo/neo}$ wave V/I ratio increase appeared
184 proportional to the degree of dysmyelination (230% and 100% increase respectively;
185 Figure 1F and 1G, bottom right). In contrast to the dysmyelination models, MCT1$^{+/-}$
186 mutants revealed no changes in threshold, latency, or amplitude of ABR waves (Figures
187 S2E to S2H). Thus, latency increase, and signal desynchronization are a result of partial
188 or complete dysmyelination, unrelated to metabolic defects.

189

Myelination of primary auditory cortex is patchy and heterogeneous

191 To study auditory processing, we first assessed the presence of myelin–in the inferior
192 colliculus (IC), an important subcortical relay station in the auditory path, and in layer 4 of
193 the primary auditory cortex (ACx), where we obtained multi-unit recordings (Figure 2A).
194 As in other grey matter areas, myelination profiles are present at low density [10,13].

195 Compared to the IC, myelination of the ACx was even sparser (Figure 2B, left upper

196 panel). In *Mbp*^{shi/shi} mice there was no compact myelin, but oligodendrocyte processes

197 loosely ensheathed the axons. Interestingly, when quantified, both *Mbp*^{shi/shi} (*shiverer*)

198 and *Mbp*^{neo/neo} mice had the same number of ensheathed axons (quantified irrespective

199 of their compaction) in the ACx as their respective controls (Figure 2B, right panels

200 graphs). Dysmyelination of *Mbp*^{neo/neo} was only obvious by electron microscopy (Figure

201 2B, lower insets). Wild type axons were surrounded by electron-dense (compact) myelin

202 (Figure 2B, left panels), *Mbp*^{shi/shi} axons were loosely ensheathed (Figure 2B, right upper

203 panel) and *Mbp*^{neo/neo} mice exhibited an intermediate profile with compact but thinner

204 myelin compared to wild type (Figure 2B, right lower panel).

205

206 **Cortical responses to simple sounds in dysmyelinated mice**

207 To study the effect of dysmyelination, we performed *in vivo* extracellular recordings in

208 *Mbp*^{shi/shi} mice (Figure 3A) following basic single sound stimuli (clicks) to evoke

209 responses. Surprisingly, at the level of the IC, we obtained an increased response

210 strength compared to controls (Figures 3B and S3A). However, at the level of the ACx,

211 response strength was similar to controls both in *Mbp*^{shi/shi} (Figures 3C and S3B, left) and

212 *Mbp*^{neo/neo} mice (Figures 3D and S3B, middle). In contrast, response latencies (Figure 3E)

213 were increased in *Mbp*^{shi/shi} at both auditory stations (Figures 3C, 3F and 3G) similar to

214 *Mbp*^{neo/neo} mice (Figures 3D and 3H), and this increase correlated with the degree of

215 dysmyelination (Figure S3B right). Response jitter (Figure S3C) and inter-trial reliability

216 (Figure S3G) were not different in any of the models or stations (Figure S3D to S3F and

217 S3H to S3J). Not surprisingly, cortical neurons in the normally myelinated MCT1^{+/-} mice

218 responded like controls to simple clicks and showed only a tendency towards longer

219 latencies (Figure S3K to S3N).

220 Changes in the ion channel distribution of the axon initial segment (AIS) are believed to

221 underlie dysmyelination-dependent changes of excitability [47]. Puzzled by the fact that the

222 hyperexcitable responses detected in the IC of *Mbp*^{shi/shi} mice were not present in the ACx

223 (Figure 3B to 3C and S3A to S3B), we measured AIS length in the ACx. Interestingly,

224 here *Mbp*^{shi/shi} mice exhibited a reduction in the lengths of AIS (Figures S4A and S4B),

225   which may explain the absence of hyperexcitable responses, as a short AIS is typically

226   associated with reduced intrinsic neuronal excitability [47–49].

227

228   **Spectral processing of pure tones**

229   Key features of spectral processing are frequency tuning and response adaptation, both

230   of which are strongly influenced by neuronal integration, i.e. the functional convergence

231   of stimuli onto individual cortical neurons. Frequency tuning, a property of the auditory

232   system, builds on frequency-specific inputs onto a given cell and is modulated by lateral

233   inhibition. Thus, differential conduction velocities in converging pathways as a result of

234   reduced myelination could have a lasting effect on neuronal integration. Surprisingly,

235   upon stimulation with pure tones (Figure 3I), tuning curves had comparable shapes in

236    $Mbp^{shi/shi}$ and wild type mice, as a function of sound intensity (Figure 3J), and covered

237   comparable best-frequency (BF) ranges within the sampled regions (Figure 3K). There

238   was no difference between groups in hearing thresholds (Figure 3L) or tuning bandwidth

239   (Figure 3M), which depends largely on convergent inputs [50].

240

241   Adaptation is crucial for sensory filtering in the auditory system [51,52] and a measure of

242   neuronal integration. It is typically tested using oddball paradigms (Figure S4C), in which

243   two frequencies that elicit responses of similar magnitude are presented sequentially such

244   that one appears with higher probability ('standard') than the other ('deviant'). Here,

245   stimulus-specific adaptation (SSA) is reflected in a decreased response to the standard

246   tone, while the response to the deviant tone remains constant or increases [52,53].

247   Importantly, cortical SSA was not reduced in $Mbp^{shi/shi}$ compared to wild type mice (Figure

248   S4D). Thus, widespread dysmyelination had no obvious effect on the integration of

249   auditory stimuli, presumably because the convergent inputs were all similarly delayed.

250

251   **Dysmyelination affects temporal reliability and acuity of sound processing**

252   Naturally occurring sounds are characterized by rich temporal structures. In many

253   species, the reliable temporal coding of communication sounds is an important factor for

254   survival or successful mating. Correct auditory coding relies on the ability of the nervous

255   system to convey the temporal structure of sounds with precise spike timing and to

256　maintain this precision while listening to continuous sound streams. We determined, on

257　one hand the neuronal capacity of our mouse models to follow click-trains (a measure of

258　temporal reliability) at different presentation rates. We also determined 'gap-detection', a

259　measure of temporal acuity, as used for audiometric testing in humans [54–56].

260

261　Click-rate detection was tested with a set of 10 clicks presented at different temporal rates

262　(Figure 4A). In wild type mice, the rates at which auditory neurons can follow were lower

263　in ACx compared to subcortical stations, consistent with a previous report [57]. Repeated

264　presentations revealed that the timing of spikes is reproducible, although failures were

265　observed in the response to the last clicks in this sequence (Figure 4B, top). Importantly,

266　in $Mbp^{shi/shi}$ mice, ACx neurons followed the initial clicks in a set of 10, but (already in the

267　5 Hz condition) revealed a strong decay in the response strength to the last clicks

268　(individual example Figure 4B, bottom). Scoring the responses to click number 1, 5 and

269　10 (taken as representatives), we observed that the response magnitude in $Mbp^{shi/shi}$ mice

270　was the same as in wild type after click 1 but was smaller after click 5 and virtually non-

271　existent by click 10 (Figure 4C). This decrease in response magnitude was associated

272　with a decreased synchrony of spiking (between repetitions along the 10 clicks) compared

273　to wild type (Figure 4D and 4E). A similar effect was observed in the cortex of $Mbp^{neo/neo}$

274　mice (Figure 4E center). Thus, 'naked' axons of $Mbp^{shi/shi}$ mice were not a prerequisite for

275　this observation. Importantly, MCT1$^{+/-}$ mice, which are normally myelinated but fail to fully

276　support axonal energy metabolism, exhibited the same deficit, which was evident at even

277　slower click rates (Figure 4E right). This suggests that axonal energy deficits are the likely

278　cause of conduction failure following repetitive neuronal firing.

279

280　The observed deficit in temporal reliability could be explained by the altered K_v channels

281　distribution (dispersed along internodes and overexpressed in $Mbp^{shi/shi}$) in axonal

282　excitable domains [58], which we confirmed in the form of shortened AIS for the ACx of

283　$Mbp^{shi/shi}$ mice at the level of the AIS (Figures S4A and S4B). In a dysmyelinated brain,

284　axonal excitability, membrane repolarization, and energy consumption could be affected

285　by the general misdistribution of ion channels [47,59]. As a model for other CNS white matter

286　tracts that are difficult to study directly, we used a well-established optic nerve preparation

287   [60]. This acute *ex vivo* system allowed us to measure compound action potentials (CAP)

288   for myelinated axons (Figure S5A) and to apply pharmacological manipulations [4,5,60]. In

289   wild type optic nerves (ON), CAPs exhibited the expected 3-peak shape, but we observed

290   strong differences with both *Mbp^{shi/shi}* and *Mbp^{neo/neo}* nerves. In these mutants, CAP peaks

291   were delayed in latency (Figure S5B) reflecting slowed nerve conduction velocity (Figure

292   S5C) proportional to the level of dysmyelination (Figures S5D). Dysmyelinated optic

293   nerves also showed a decrease in peak amplitude (Figure S5B) and CAP area (Figure

294   S5G), suggesting conduction blocks in the ON, and we noted an increase of the

295   hyperpolarizing phase with a larger negative CAP area (Figure S5H). These features

296   were similar to CAP recordings from the spinal cord of *Mbp^{shi/shi}* mice [58]. To test our

297   hypothesis that excess potassium fluxes in dysmyelinated *Mbp^{shi/shi}* optic nerve axons

298   cause energy loss (due to repolarization-associated ATP consumption) and contribute to

299   reduced temporal reliability, we blocked potassium channels with 4-aminopyridine (4-AP,

300   25 µM) in a bath application. This treatment normalized the CAP amplitude and

301   decreased the hyperpolarizing phase of *Mbp^{shi/shi}* axons (Figures S5F gray, S5G

302   rightmost and S5H rightmost). This finding is compatible with abnormal ion fluxes in the

303   mutant axons, which increase ATP consumption and cause abnormal repolarization

304   dynamics.

305

306   The second key aspect of auditory processing is temporal acuity. Gap-detection protocols

307   measure the ability of neurons to detect short silent gaps in the middle of a white noise

308   sound (Figure 5A), a capacity also crucial in human speech processing [61]. In mice, the

309   presence and the strength of any post-gap sound response reflects whether the gap has

310   been detected (Figure 5B). *Mbp^{shi/shi}* mice revealed a significant decrease (compared to

311   wild types) in their post-gap response strength for gaps shorter than 3 ms in duration

312   (Figures 5B and 5D). Quantification of this effect (by comparing for each recording the

313   ratio between baseline activity and post-gap activity) confirmed that the cortical neurons

314   of *Mbp^{shi/shi}* mice failed to detect small gaps (Figure 5C). A milder but similar effect was

315   observed in *Mbp^{neo/neo}* mice (Figures 5E, S6A and S6B), suggesting that these temporal

316   acuity deficits reflect the level of dysmyelination. Importantly, MCT1$^{+/-}$ mice revealed only

317   very minor gap detection deficit compared to their respective controls (Figures S6C to

318   S6E). Thus, loss of temporal acuity must be attributed to hypomyelination, rather than

319   reduced metabolic support of the axonal compartment.

320

321   **Behavioral correlates of reduced temporal acuity**

322   To understand the correlation between gap-detection deficits and perception at the

323   behavioral level we performed two tests in behaving mice. First, we tested 'gap-

324   dependent pre-pulse inhibition of the acoustic startle reflex' (GDIASR). This paradigm is

325   widely used to behaviorally assess the detection of gaps within sound stimuli [62–65]. For

326   this test we could only use hypomyelinated $Mbp^{neo/neo}$ mice that have no motor defects.

327

328   Pre-pulse inhibition of the acoustic startle reflex (ASR) requires sensorimotor gating.

329   Acoustic startles are triggered by a loud unexpected sound [66] and can be measured by a

330   piezo element under the animal (Figure S7A). A change in the sound background, for

331   example a 'silent gap' just before the starling sound (Figure 6A), can inhibit the ASR if it

332   is salient enough [67]. In this paradigm, we used the level of inhibition by different 'silent

333   gap' lengths (Figure S7B) as a behavioral measure of gap-detection (i.e. gap perception).

334   Consistent with previous reports from wild type mice [62,65,67,68], shorter gaps elicited less

335   inhibition than longer gaps (Figure 6B). Importantly, dysmyelinated $Mbp^{neo/neo}$ mice

336   showed a significant decrease in the inhibition of the ASR, when triggered by different

337   gap lengths. Moreover, we determined a two-fold increase in the gap detection threshold

338   (from 8 ms to 17 ms) (Figure 6B and 6C). Thus, deficits in temporal acuity, discovered at

339   the physiological level in the ACx, were also paralleled at the perceptual level. We note

340   that mice with slightly higher levels of Mbp expression, i.e. thinly myelinated heterozygous

341    $Mbp^{shi/+}$ mutants, did not show a reduction in basic startle or in gap-perception (Figures

342   6B, 6C, S7C and S7D). Thus, significant hypomyelination (>50%) is required to elicit gap-

343   detection deficits at the behavioral level.

344

345   To confirm altered gap perception in freely behaving mice, we tested $Mbp^{neo/neo}$ mutants

346   in the 'AudioBox' (New$Behavior$, TSE systems), an automated system for auditory

347   behavioral testing [69–73]. Animals were exposed to 'safe visits' of one cage corner (Figure

348   S7E), in which a continuous sound was played, and water was always available.

349 However, during 'conditioned visits' of that corner the continuous sound was interrupted
350 by a series of 50 ms 'silent gaps' that were paired (i.e. negatively conditioned) with short
351 air-puffs to the nose when animals attempted to drink. We then compared the sensitivity
352 to different gap lengths in mutants and controls ranging between 1 and 45 ms (Figures
353 6D and S7F). For each gap length we quantified the percentage of visits in which the mice
354 avoided penalized nose-pokes, indicating perception of this gap. Despite equivalent
355 sound exposure in the Audiobox (Figure S7G), gap detection threshold was increased to
356 4 ms in $Mbp^{neo/neo}$ compared to the 2 ms threshold of wild type mice (Figure 6E). We
357 conclude that in freely moving animals, myelination contributes to auditory perceptual
358 acuity.

359

360 **Discussion**

361 To explore the role of CNS myelination in information processing, i.e. beyond the known
362 function of myelin in speeding axonal conduction, we studied the detection and perception
363 of auditory stimuli in mice. We used auditory brainstem potentials and multiunit recordings
364 in the auditory cortex of mutant mice, as well as behavioral readouts in awake animals,
365 to compare the effect of partial ($Mbp^{neo/neo}$) and complete ($Mbp^{shi/shi}$) dysmyelination with
366 that of an isolated reduction of glial metabolic support ($MCT1^{+/-}$). The combined pattern
367 of results reveals that diminished glial support of axonal metabolism, in the absence of
368 dysmyelination, impairs sustained stimulus detection relevant for speech processing. The
369 deficits were largely comparable, although partially discriminable from those resulting
370 from dysmyelination. Oligodendrocytes, therefore, play an important role in ongoing
371 perception through energetic support (Figure 7A), most evident when dysmyelination
372 results in misdistribution of axonal ion channels (Figure 7B), and independent of a role in
373 saltatory conduction. (Figure 7C).

374

375 On the other hand, subcortical delays in dysmyelinated mice were accompanied by
376 reduced synchrony of auditory brainstem potentials, a feature not observed in mice with
377 only reduced glial metabolic support. The decreased amplitudes and shapes of waves II
378 and III, were likely reflecting some desynchronization of the converging input at the level
379 of the cochlear nucleus and olivary complex (where ascending auditory signals become

380   bilateral). The later waves IV and V showed instead an increase in size in dysmyelinated

381   mutants, most likely reflecting a compensatory mechanism to the loss of synchrony at the

382   earlier stations. Similarly gain increases have been reported in mice deprived of auditory

383   stimuli [74], and in humans as a result of aging [44] or multiple sclerosis lesions [7,75–78].

384

385   While dysmyelination had a strong effect on conduction velocity, spectral processing of

386   simple stimuli (pure tones) in the primary auditory cortex appeared normal. Auditory

387   information can reach the IC and then the ACx through different parallel pathways, each

388   of which might be differently affected by dysmyelination. While simple click sounds, and

389   pure tones are likely activating a limited (possibly the most direct) subset of sound

390   encoding circuits, responses to these stimuli were normal, indicating that basic relay

391   processing and sound integration is not affected by the absence of myelin. However, we

392   detected deficits in temporal processing in a manner unexplained by reduced conduction

393   velocity alone. Temporal reliability and acuity were affected in all mutants. Unexpectedly,

394   the magnitude of this defect was correlated with the degree of hypomyelination but was

395   not limited to dysmyelination phenotypes. It was also a feature of MCT1$^{+/-}$ mice with an

396   isolated metabolic support defect. Behavioral tests demonstrated that the temporal

397   processing deficits, as detected by cortical multi-unit recordings, were paralleled at the

398   perceptual level. Myelinating oligodendrocytes are thus clearly involved in the temporal

399   processing of auditory signals, which have previously been implicated in higher CNS

400   functions in humans, such as speech recognition [79–81]. Here, the phenotypical similarities

401   of two different mouse mutants, *Mbp^{neo/neo}* and MCT1$^{+/-}$, suggest that compromised

402   metabolic support alone is a critical component of reduced myelination and becomes

403   detectable at the network level in the absence of any sign of axonal degeneration.

404

405   Myelination defects clearly affected the coding of a stimulus' temporal envelope, reflected

406   for example as 'fatigability', i.e. a lack of temporal reliability. For *Mbp* mutants it was

407   unexpected that the responses to longer trains of clicks diminished or even stopped after

408   5 to 6 repetitions of the stimulus, especially when the intervals between consecutive clicks

409   were 200 ms apart (repetition rate 5 Hz). Here, the altered distribution of sodium and

410   potassium channels in unmyelinated regions is critical. In *Mbp^{shi/shi}* mice sodium channels

411   are increased along bare axons [82,83], and abnormally high expression of $Na_v1.2$ channels

412   does not revert to $Na_v1.6$ in development [84,85]. This might contribute to increased

413   fatigability in $Mbp^{shi/shi}$ mice since $Na_v1.6$ channels are not only associated with - but also

414   necessary for - repetitive firing [86]. In addition, an elongation of nodes [58,87] and

415   overexpression of $K_v1.1$ and $K_v1.2$ potassium channels has been reported in *shiverer*

416   mice [58,88]. K_v1 channels are normally clustered at juxtaparanodal domains [89] but may

417   become abnormally exposed to the extracellular space upon dysmyelination and

418   redistribute into the paranodal and internodal membrane causing increased K_v1-mediated

419   potassium efflux. In the absence of myelin, oligodendrocyte-dependent potassium

420   siphoning would be reduced [90]. Together, this might lead to a greater activity-driven

421   accumulation of extracellular potassium, decreasing its driving force and resulting in a

422   longer time course of membrane hyperpolarization. In agreement with these findings,

423   when potassium channels in *shiverer* mice were acutely blocked with 4-AP in the *ex vivo*

424   electrophysiological recordings of $Mbp^{shi/shi}$ optic nerves (our accessible model of a

425   dysmyelinated tract), we noted a partial restoration of single compound action potential

426   (CAP) amplitude and a smaller hyperpolarization phase. The latter is consistent with the

427   efficiency of 4-AP as a symptomatic treatment for MS [91].

428

429   Interestingly, reduced reliability was also observed in the MCT1$^{+/-}$ mice, without

430   dysmyelination, suggesting that reduced metabolic support to axons might be one of the

431   responsible mechanisms. An indirect effect, and not necessarily an alternative

432   explanation to the channel misdistribution, is the burden of dysmyelination and increased

433   ion fluxes on the energy consumption of axonal Na^+/K^+ ATPases, postulated to be a

434   contributing factor to axonal degeneration in demyelinated plaques of multiple sclerosis

435   (MS) [92]. Indeed, hearing difficulties have been reported also in MS patients [78]. In the *Mbp*

436   mutants, inadequate support might occur locally but have a dominant effect on the entire

437   pathway. For example, lack of myelin might reduce energy reserves at higher spiking

438   rates when the ATP-dependent ion pumps are most active. This might cause conduction

439   blocks in the absence of axonal degeneration.

440

441   In addition to some loss of 'temporal reliability', we determined a myelination dependent

442   defect of 'temporal acuity', i.e. a defect in the coding of rapid changes in the temporal

443   structure of the stimulus. Here, a powerful paradigm is sound gap-detection [54,93], a

444   function that relies on cortical auditory processing [65,94–96]. In humans, defects in such a

445   gap detection test are closely associated with a corresponding loss of accurate speech

446   discrimination [97,98]. Cortical neurons of dysmyelinated *shiverer* mice failed to detect silent

447   gaps within a stream of white noise when these gaps were shorter than 3 ms, a marked

448   deviation from control mice that detect gaps as short as 0.5-1 ms. Hypomyelinated

449   *Mbp*$^{neo/neo}$ mice exhibited a milder deficit.

450

451   Poor gap detection in *Mbp*$^{shi/shi}$ mice could be caused by longer refractory periods and

452   reduced excitability of the axons secondary to ~~the~~ abnormal distribution of ion channels.

453   It would explain why these deficits in temporal acuity were less severe in the

454   hypomyelinated *Mbp*$^{neo/neo}$ mice. In contrast, neuronal 'fatigue' and the loss of temporal

455   reliability are both caused by an underlying metabolic problem that is also prominent in

456   MCT1 heterozygotes.

457

458   All multi-unit recordings were performed in anaesthetized mice. We note that key aspects

459   of auditory processing occur 'pre-attentively' and should be unaffected by anesthetics [99].

460   However, neuronal circuits with inhibitory input can behave differently under anesthesia,

461   which can bias experimental results. Thus, it was important to parallel the

462   electrophysiological results with behavioral experiments on auditory perception in freely

463   moving animals. Since motor impaired *Mbp*$^{shi/shi}$ mice could not be used for these

464   experiments, we analyzed mice homozygous for the newly created *Mbp*$^{neo/neo}$ allele,

465   which had no visible motor defects and were long-lived. In this mutant, we confirmed poor

466   gap detection at the perceptual level by operant conditioning of auditory stimuli and

467   responses. We observed no such auditory deficits in heterozygous *shiverer* mice, which

468   exhibit a minor dysmyelination [36]. This suggests that a threshold level of hypomyelination

469   is required for the auditory phenotype.

470

471　It has become increasingly clear that the role of myelination is not limited to speeding
472　axonal conduction velocity. Moreover, the patchy myelination pattern of cortical circuits
473　points to a broader role of oligodendrocytes and myelin in information processing [100]. Our
474　mouse models with predominant structural or metabolic defects of CNS myelin allowed
475　exploring the role of myelination at the network level. This enabled us to mechanistically
476　dissect reliability defects from acuity deficits in auditory processing. Thus, our studies
477　revealed a novel role of myelin forming oligodendrocytes in information processing that
478　goes beyond the speeding of neuronal responses. We discovered that myelin influences
479　the sustained and temporally precise axonal firing, essential to properly code auditory
480　stimuli. Moreover, specific phenotypical similarities between mutants with dysmyelination
481　and metabolic defects suggests that a myelin-dependent energetic failure marks a
482　common mechanism underlying auditory dysfunctions. Auditory phenotyping emerges as
483　a promising experimental system to investigate the role of oligodendrocytes and
484　myelination in information processing.

485

486　**Methods**

487　**Mice**

488　All mice were housed in standard plastic cages with 1-5 littermates in a 12 h/12 h light/dark cycle
489　(5:30 am/5:30 pm) in a temperature-controlled room (~21°C), with *ad libitum* access to food and
490　water. All mice used were bred under the C57BL6/N background. Data obtained from male and
491　female mice were pooled unless otherwise stated. The experimental and surgical procedures
492　were approved and performed in accordance with the Niedersächsisches Landesamt für
493　Verbraucherschutz und Lebensmittelsicherheit (licence number 33.19-42502-04-16/2337).

494

495　Homozygous *shiverer* mice were obtained by crossing heterozygotes (*Mbp$^{shi/+}$*). In all
496　experiments, *Mbp$^{shi/shi}$* mice and their control littermates (Wt) were 6-12 weeks of age, unless
497　otherwise stated.

498

499　A new hypomyelinated mouse with reduced *Mbp* expression (<50%), was generated by
500　homologous recombination in ES cells, using a modified *Mbp* gene carrying a LacZ-neomycin
501　cassette upstream of exon 1. Successful targeting disrupted the 5' regulatory region without
502　affecting the larger GOLLI transcription unit (Figure S1A). Homozygous *Mbp$^{neo/neo}$* mice were born

503   at the expected frequency. For all experiments, *Mbp^{neo/neo}* and controls (Wt) were used at age 9.5-

504   14 weeks, unless otherwise stated.

505

506   MCT1$^{+/-}$ mice, with reduced axo-glial metabolic support [3] were kindly provided by Pierre

507   Magistretti (Lausanne) and analyzed at age 10-14 weeks.

508

509   **Acoustic stimulation**

510   All sound stimuli were digitally synthesized and presented using Matlab (The Mathworks®, USA),

511   at a sampling rate of 98 kHz and in a pseudorandom order. There were typically 10 repetitions of

512   each stimulus, unless otherwise stated. The intensities were measured in decibel sound pressure

513   levels (dB-SPL). Sounds used for electrophysiology were delivered by an USB audio interface

514   (Octa-capture, Roland, USA), amplified with a Portable Ultrasonic Power Amplifier (Avisoft,

515   Germany) and played in a free-field ultrasonic speaker (Ultrasonic Dynamic Speaker Vifa, Avisoft,

516   Germay). Calibration of the testing apparatus was made using BBN and click sounds at different

517   intensities with a Brüel & Kjaer (4939 ¼") free field microphone, with Brüel & Kjaer amplifier

518   (D4039, 2610, Denmark). All experiments were performed in a sound-attenuated and anechoic

519   room.

520

521   **Auditory Brainstem Responses**

522   Auditory brainstem responses (ABRs) were measured as described [101]. Mice were anesthetized

523   with an intraperitoneal injection of 250 mg/kg Avertin (mixture of 2,2,2-tribromoethyl alcohol 2%,

524   Sigma-Aldrich, and tert-amyl-alcohol 2%, Merck), except for the Mbp^{neo/neo} line, which was treated

525   as in Jung et al. (2015) [102] and anesthetized with ketamine (125 mg/kg) and xylazine (2.5 mg/kg)

526   i.p. Temperature was kept at 36° via a heating pad (World Precision Instruments, ATC 1000). For

527   the recordings, subdermal needles (BD Microlance, 30G ½", 0.3x13mm) were placed at the vertex

528   (active electrode), the left pinna (reference) and the back of the animal (active shielding). Click

529   stimuli were ipsilaterally delivered from a speaker located ~9 cm from the left ear. Square click

530   waveforms (0.03 ms long) were presented at 20 Hz (50 ms inter-trial intervals (ITI)) at different

531   intensities (0-80 dB). The difference in potentials was amplified 10,000 times using a custom-

532   made amplifier. A National Instruments shielded I/O connector block (NI SCB-68), interfaced in a

533   Matlab environment was used for data acquisition (50,000 Hz sampling rate). Recorded voltage

534   traces were bandpass filtered offline (300 - 3000 Hz) using a Butterworth filter. Data was cut from

535   the stimulus presentation onset (0 ms) in 12 ms windows. Trials with heart rate artifacts (wave

536   shapes larger than ± 4.7-9.2 μV) were removed, and 1000 trial repetitions of each stimulus were

537 used for data analysis. Hearing thresholds were determined as the lowest intensity that evoked a
538 response that was 3 times the root mean square of the response at 0 dB within a window of 1 ms
539 centered on wave I. In addition, this measurement was confirmed by visual inspection of the
540 lowest intensity that evoked a response (compared to 0 dB) within 6 ms from stimulus onset. The
541 identity of the waves was determined by visual selection of the maximum peak value
542 corresponding to each of the five waves according to the typical reported position of each wave
543 (1 ms apart). For the analysis, an ANOVA was used to assess the changes in latencies or
544 amplitudes of each wave, comparing control to mutant animals.

545

546 **Electron microscopy**
547 After transcardial perfusion fixation (4% formaldehyde and 2.5% glutaraldehyde in phosphate
548 buffer), mouse brains were dissected, and sagittal or coronal vibratome (Leica VT1000S) slices
549 of 200-300 μm thickness were prepared. A punch of the region of interest was taken, prepared
550 for electron microscopy [103] and embedded in Epon. Ultrathin sections were prepared using a Leica
551 Ultracut S ultramicrotome (Leica, Vienna, Austria) and imaged with a LEO912 electron
552 microscope (Zeiss, Oberkochen, Germany) using a 2k on-axis CCD camera (TRS, Moorenweis,
553 Germany). G-ratios (axonal diameter/fibre diameter) were determined by analyzing 100 axons
554 per animal selected by systematic random sampling on 10 random images taken at a
555 magnification of 8,000 x.

556

557 **Acute electrophysiology**
558 Prior to surgery, mice were anesthetized and maintained as reported for the ABR procedure. Mice
559 were placed on a stereotaxic apparatus using inverted ear bars to avoid damage to the ear canal
560 (World Precision Instruments, Sarota, FL USA, 502063). A cut was made along the midline and
561 the skull exposed and cleaned of adherent tissue with a scalpel and hydrogen peroxide. A metal
562 screw (M1x1, Germany) was inserted into the right parietal cortex and used as ground. A metal
563 post was glued on the skull frontal to lambda with dental cement (Unifast, TRAD), this allowed for
564 removal of the ear bars. The muscle temporalis was detached from the skull and a 4x2 mm
565 craniotomy was performed using a dental drill (World Precision Instruments, Omnidrill3, tip #7),
566 following the contour delimited rostral and ventrally by the squamosal suture, dorsally by the
567 temporal ridge and caudally by the lambdoid suture. The speaker was placed ~13 cm from the
568 right ear of the mouse. At the end of every experiment, mice were euthanized by anesthesia
569 overdose. The brain was removed, and immersion fixed in 4% PFA. After 24h, the brain was
570 washed with PBS 1x and stored in 30% sucrose (Merk, K43386951).

571

572 Recordings were performed with glass-covered tungsten electrodes (AlphaOmega, Germany) or

573 platinum/tungsten glass coated electrodes (Thomas Recordings, Germany) with impedances

574 between 1.5 and 2 MΩ. In 30% of the recordings, the electrode was stained with Dye I

575 (dioctadecyl-tetramethylindocarbocyanine perchlorate, Aldrich, 468495) dissolved in absolute

576 ethanol, before insertion, for later visualization of its position. After the craniotomy, a drop of saline

577 was used to clean the surface of the brain. The electrode was inserted perpendicular to the

578 surface of the primary auditory cortex [104] using a micromanipulator (Kopf, Inc., Germany). We

579 recorded extracellular multi-unit (MUA) sound-evoked responses in layer 3/4 of the ACx of

580 anesthetized mice. Responses were characterized by onset latency and shape. ACx recordings

581 in $Mbp^{shi/shi}$ mice were done at a depth of ~405 μm (62 μm standard deviation (sd)) without

582 differences in depth between control and mutant mice (p=0.71). In the $Mbp^{neo/neo}$ line, depth of

583 recording was on average ~350 μm (60.5 μm sd) without differences between groups (p=0.520).

584 In MCT1$^{+/-}$ mice, recordings were on average at ~380 μm depth (37 μm sd) (p=0.32).

585

586 Electrophysiological signals were acquired at 32 kHz sampling rate, pre-amplified (HS-36-Led,

587 Neuralynx, USA) and sent to an acquisition board (Digital Lynx 4SX, Neuralynx, USA) to yield the

588 raw signals, which were acquired using a bandpass filter (0.1 or 200 Hz to 9000 Hz) and stored

589 for offline analysis. Recording and visualization of the data was made using the Cheetah Data

590 Acquisition System software (Neuralynx, USA). For multi-unit analysis (MUA), spikes that are not

591 attributed to a single neuron, the signals were high-pass filtered at 350 Hz. For spike detection, a

592 threshold of 6 times the mean absolute deviation from the median of the filtered voltage traces

593 was used. For the analysis, only recordings that had significant auditory evoked responses at any

594 sound intensity compared to a 200 ms pre-sound baseline activity (paired t-test) were used.

595

596 To measure tonotopy, *pure tones* of variable frequencies and intensities were presented (24 tones

597 with frequencies between 2 to 31 kHz, and intensities between 0 and 80 dB) (Figure 3I). Each

598 tone was 30 ms long, had on/off ramps of 5 ms. Presentation rate was 2 Hz (500 ms inter-trial

599 interval). Five repetitions of each frequency/intensity combination were presented in a random

600 order. The analysis was performed on individual recording sites, although in many mice

601 recordings were obtained from several site along the ACx.

602

603 For the reconstruction of the single-site tuning (Figure 3J), the spikes elicited by each frequency

604 in a 200 ms window after stimulus onset were added. The tuning curves (TC) were smoothened

605   using a zero-phase digital hamming filter with a window of 4 points. The smoothened TC were

606   then used to calculate the best frequency (BF; the frequency that elicited the maximum number

607   of spikes at 60 and 80 dB). In normalized tuning curves, activity was expressed as a function not

608   of frequency but of the distance (in octaves) from the best frequency. Response thresholds were

609   obtained by visual inspection (blinded as to the genotype) of a 200 ms window from stimulus

610   onset. Tuning curve width both at the base and the half distance from the peak activity (Figure

611   3M), was calculated as the z-score of the sum of spikes over a 60 ms window from stimulus onset

612   at all frequencies and intensities.

613

614   The *click rate* (CR) protocol (Figure 4A) was used to assess temporal reliability. Each was a 0.05

615   millisecond long positive step function. Bursts of ten clicks were presented every 6 s, each at a

616   different rate (2 - 50 Hz). The first click of each burst was used to characterize latency, amplitude,

617   reliability and jitter of auditory response (Figure 3 and S3). For the *latencies* measurement we

618   only included the spikes that occurred at least 10 ms after sound onset, given latencies reported

619   for the ACx in anesthetized mice [104]. To measure reliability of repeated responses (click rate

620   protocol, Figure 4), synchronicity measurements were obtained from a measure of the vector

621   strength [105] of the spikes occurring for the duration of the stimulation in all repetitions of the

622   stimulus was obtained by converting each spike time (τ_i) as a circular vector with phase (θ_i)

623   between 0 and 2π, according to the stimulus phase of a specific rate. All the spikes occurring after

624   each of the 10 clicks were selected in terms of their latency respective to the previous click. A

625   window equivalent to the phase duration (equal to the inter-click interval) was selected for each

626   click rate presentation. The spike phases were then expressed in terms of:

627   **Equation 1**

628
$$\theta_i = 2\pi \frac{\mathrm{mod}(\tau_i, \rho)}{\rho}$$

629   Here, τ_i is the latency of each spike, θ_i was the phase representation of each spike, and ρ was

630   the phase of the stimulus presented (for example for a click train at 5 Hz, $\rho = \frac{1}{5}$, $\rho=0.2$). To calculate

631   the percentage of spike synchronicity, the total spike phase distribution was binned in 20 bins

632   from 0 to 2π, and the spike count of the bin with the maximum synchronization in the first half of

633   the vector (π), was taken. This spike count was expressed in terms of percentage, which means

634   the percentage of spikes that were fully synchronized per stimulus in one recording.

635

636   The *gap-in-noise detection* paradigm was used to evaluate temporal acuity. Once every second,

637   200 ms long broad band noise (BBN, pre-gap) sound was followed, after a short silent gap, by a

638   50 ms long BBN sound (post-gap). Silent gaps durations were 0, 0.5, 1, 2, 3, 4, 5, 7, 10, 20, 50

639   and 100 ms (Figure 5A). Rise/fall time of the BBN pulse was 1 ms. For *gap-detection* analysis,

640   only recordings with a significant response to the mean of the pre-gap sound (sum of spikes over

641   100 ms window after stimulus onset), compared to pre-sound baseline, were used (paired t-test).

642   For each animal, recordings at different locations were averaged. Additionally, only those animals

643   that had a significant response to the post-gap BBN following a 100 ms gap were included in the

644   analysis (100 ms window from the start of the post-gap BBN). Peri-stimulus time histograms

645   (PSTH) were generated by adding spikes across trials in 1 ms bins over a 100 ms window (Figure

646   5D). The pre-gap response (PSTH in a 100 ms window) was generated from all gap trials, since

647   the pre-gap response should not be affected by the gap that follows it. For the post-gap responses

648   (PSTH over 100 ms), each gap was treated separately. Comparisons between control and

649    $Mbp^{shi/shi}$ and $Mbp^{neo/neo}$ mice revealed no significant differences in the amplitude of the pre-gap

650   response (ANOVA, p=0.53 and p=0.6 respectively). Also, the peak of the post-gap response was

651   used for group comparisons. Since some groups showed increased latencies, the PSTHs were

652   centered at their peaks. An ANOVA was performed in a 21 ms window centered on the peak.

653

654   For the analysis of the gap-detection *vs* baseline, a 50 ms window of baseline activity was

655   compared to a 50 ms window of the post-gap response for each recording site using a paired t-

656   test.

657

658   **Gap pre-pulse inhibition of the acoustic startle reflex**

659   We used behavioral Gap-PPI to test behavioral temporal acuity [67]. This test was performed in

660    $Mbp^{neo/neo}$, $Mbp^{shi/+}$ and their control littermates. We used 9 control animals (wild types pulled

661   together from both dysmyelination lines), 6 $Mbp^{neo/neo}$, 6 $Mbp^{shi/+}$. All mice were between 9 and 16

662   weeks at the age of testing. For testing, a mouse was confined in a custom-made Plexiglas tunnel

663   (12 cm long by 4 cm diameter), placed above a piezo element (TRU components, 800 Ohms

664   impedance, 50 mm diameter, spanning 30V) (Figure S7A). The piezo was connected to a data

665   acquisition system (NI SCB-68). Data acquisition (1 kHz sampling rate) was controlled with a

666   custom-made code in a Matlab and sound delivery was done using pre-synthetized sound tracks

667   in Matlab, played through VLC media player (Video Lan Organization).

668

669   Testing protocol was as summarized in Figure S7B. Mice were initially acclimatized to the setup

670   for 10 min before the start of the experiment: 5 min. of silence followed by 5 min. of exposure to

671   the background sound (BBN of 70 dB). Testing was then initiated. The startle noise was a BBN

672   105 dB with 40 ms duration. It appeared every 10-20 s. at random times to avoid startle prediction.

673   The startle could be preceded by a gap (0, 1, 2, 3, 5, 7, 10, 25 or 50 ms long) which ended 50 ms

674   before the startle (Figure 6A). Gaps and startle had on/off ramps of 1 ms. The session started

675   with 10 startle-only pulses, followed by gap preceded startle presentations (10 startle presentation

676   per gap type). The experiment ended with five startle-only pulses, to assess habituation. The

677   complete presentation of 105 trials had a duration of approximately 30 min.

678

679   *Gap-PPI* analysis was done as described before [67], with mild modifications. The magnitude of the

680   acoustic startle reflex (ASR) was measured as the maximal vertical force (peak-to-peak voltage

681   output) exerted on the piezo element in a 500 ms window starting with the onset of the startle

682   noise. Baseline activity (2 times the root mean square of the voltage trace in a 500 ms window

683   before the startle noise) was subtracted. Startle and baseline amplitude were measured in

684   arbitrary voltage units provided by the piezo measurement. Noisy trials (3 times the standard

685   deviation of the root mean square of a 500 ms window before gap presentation) were discarded

686   from the analysis. The percentage of pre-pulse inhibition for each gap and mouse was calculated

687   following:

688   **Equation 2**

689
$$PPI(\%) = 100 \frac{ASR - ASRx}{ASR}$$

690   Where ASR is the startle response elicited at 0 ms gap, and ASRx is the startle response elicited

691   per gap played. The data were fitted with a generalized logistic function:

692   **Equation 3**

693
$$f = -\frac{a}{2} + \frac{a}{1 + exp(b + c * x)}$$

694   Recordings with a fit coefficient (R^2) below 0.6 were excluded from the analysis.

695

696   The gap detection threshold was considered as the value of the fitted curve that elicited

697   50% of the maximal inhibition achieved per mouse. A second normalization was then made to the

698   longest gap (50 ms) presumed to elicit the maximum value of inhibition (100%). For the statistical

699   comparisons of the gap-detection threshold and amplitude of startle, parametric or non-parametric

700   t-test were used. A 2-way ANOVA was performed for the comparison of the inhibition of the ASR

701   along the different gap lengths.

AudioBox

The AudioBox system was used to test behavioral gap-detection. The AudioBox (New*Behavior*, TSE systems) is an automated system for behavioral acoustic conditioning [69–72]. This system is designed to minimize the interference from the experimenter and provides a spatially and socially enriched environment in which female mice live in group (up to 10 mice) for several days**.** The setup consisted of a home-cage, where animals had food *ad-libitum,* and a corner within a sound-attenuated box, where they could access water also *ad-libitum* (Figure S7E). A speaker was over the corner (22TAF/G, Seas Prestige). Animals carried a transponder (implanted under anesthesia, see [72]) that was detected by an antenna at the entrance of the corner. Time spent in the corner, number of nose-pokes and sound played were detected through sensors in the corner.

For these experiments, $Mbp^{neo/neo}$ mice were chosen over $Mbp^{shi/shi}$ because of their normal life span and lack of motor impairments. Three experiment replications were pooled together. A final number of 7 control animals (Wt) and 13 mutant animals ($Mbp^{neo/neo}$) that were 6-14 weeks old at the start of the experiment were used.

Behavioral testing occurred in the corner. Each time a mouse entered the corner a "visit" started, and a sound was played for the duration of the visit. The training paradigm, summarized in Figure S7F, consisted of 3 phases. During the habituation (one day doors opened, and 3-9 days doors closed), the safe sound (continuous BBN) was played in all visits. In this phase, animals could nose-poke and get access to water. During the conditioning phase 'conditioned' visits were introduced (Figure 6D and S7F). In safe visits, as before, the animal could make a nose-poke and get water. Animals that did not nose-poke in more than 60% of safe visits were immediately excluded from the behavioral experiment. This was the case for 11 out of a total of 18 Wt and 7 out of 20 $Mbp^{neo/neo}$ tested. In conditioned visits (pseudo-randomly distributed according to probabilities as in Figure S7F), however, a conditioned sound (BBN interrupted by 50 ms silent gaps every 500 ms) was played, and a nose-poke triggered an air-puff, and no opening of the doors. Mice had to learn to not nose-poke in visits in which silent gaps interrupted the sound. Typically, this occurred 1-2 days after introduction of the conditioned visits. The percentage of conditioned sound presentation was increased stepwise 5% every 2 days. After the conditioning phase, the gap testing phase began. Every 4 days two new visit types were introduced, each with BBN sounds interrupted, like the conditioned sounds, by gaps, which varied in length with visit type (Figure 6D and S7F). During this phase 70% of visits were safe, 20% conditioned and 10% conditioned gaps. A total of 15 gaps were tested with lengths between 1 and 45 ms.

735   The new sounds were chosen in pairs in a semi-random fashion, such that the more difficult gaps

736   (gaps below 5 ms) were presented in the same block of days as gaps longer than 5 ms. A

737   minimum of four days with each pair of sounds was allowed before starting a new gap testing.

738

739   The percentage of avoidance was quantified as the number of visits without nose-pokes for each

740   sound played, only considering the first two days of training for each sound. The number of visits

741   was compared to ensure equivalent sound exposure. The data from visits with gaps between 2

742   and 15 ms duration were used for statistical comparison.

743

744   **Analysis generalities**

745   Analyses and figure outputs were always performed in a Matlab environment. All confidence

746   intervals correspond to $\alpha=0.05$. Significance corresponds to [n.s.]$p>0.05$, *$p\leq0.05$, **$p\leq0.01$,

747   ***$p\leq0.001$, ****$p\leq0.0001$. Statistical analysis was parametric or non-parametric according to the

748   Shapiro-Wilcoxon normality test.

749

750   Paired comparisons were done using t-test or ranksum and post-hoc multiple comparisons

751   were performed using 2-way ANOVA or Kruskal-Wallis.

752

Acknowledgements

Author contributions

Conceptualization, L.dH. and S.M.; electron microscopy images, T.R. and W.M.; ABR recordings of *Mbp^{neo/neo}*, N.S.; ABR recordings, *in vivo* electrophysiology, and behavior, S.M.; *in vivo* electrophysiology for SSA, L.d.H.; generation, cellular and molecular characterization of the *Mbp^{neo/neo}* model, W.M., and M.M.; AIS stainings and quantification, I.T., A.B., and M.K.; ON recordings, S.M., and A.T.; maintenance of MCT1 mice, K.K.; data analysis, S.M., and L.dH.; data curation, S.M.; writing-original draft, S.M., L.dH., and K.A.N; revision-editing, all authors; funding acquisition, S.M., L.dH., and K.A.N; project supervision, L.dH., and K.A.N.

Declaration of interests

The authors declare no competing interests.

References

1. Nave, K.-A. & Werner, H. B. Myelination of the nervous system: mechanisms and functions. *Annu. Rev. Cell Dev. Biol.* **30,** 503–533 (2014).

2. *Fünfschilling, U. et al. Glycolytic oligodendrocytes maintain myelin and long-term axonal integrity. Nature* **485,** *517–521 (2012).*

3. *Lee, Y. et al. Oligodendroglia metabolically support axons and contribute to neurodegeneration. Nature* **487,** *443–448 (2012).*

4. *Saab, A. S. et al. Oligodendroglial NMDA receptors regulate glucose import and axonal energy metabolism. Neuron* **91,** *119–132 (2016).*

5. *Trevisiol, A. et al. Monitoring ATP dynamics in electrically active white matter tracts. Elife* **6,** *(2017).*

6. *Nave, K.-A. & Ehrenreich, H. Myelination and oligodendrocyte functions in psychiatric diseases. JAMA Psychiatry* **71,** *582–584 (2014).*

7. *Peters, A. The effects of normal aging on myelinated nerve fibers in monkey central nervous system. Front. Neuroanat.* **3,** *11 (2009).*

8. *Peters, A., Sethares, C. & Killiany, R. J. Effects of age on the thickness of myelin sheaths in monkey primary visual cortex. J. Comp. Neurol.* **435,** *241–248 (2001).*

9. *Stange-Marten, A. et al. Input timing for spatial processing is precisely tuned via constant synaptic delays and myelination patterns in the auditory brainstem. Proc. Natl. Acad. Sci. USA* **114,** *E4851–E4858 (2017).*

10. *Tomassy, G. S. et al. Distinct profiles of myelin distribution along single axons of pyramidal neurons in the neocortex. Science* **344,** *319–324 (2014).*

11. *Gao, R. et al. Cortical column and whole-brain imaging with molecular contrast and nanoscale resolution. Science* **363,** *(2019).*

12. *Stedehouder, J., Brizee, D., Shpak, G. & Kushner, S. A. Activity-Dependent Myelination of Parvalbumin Interneurons Mediated by Axonal Morphological Plasticity. J. Neurosci.* **38,** *3631–3642 (2018).*

13. *Micheva, K. D. et al. A large fraction of neocortical myelin ensheathes axons of local inhibitory neurons. Elife* **5,** *(2016).*

14. *Zonouzi, M. & Berger, D. Individual Oligodendrocytes Show Bias for Inhibitory Axons in the Neocortex.*

15. *Demerens, C. et al. Induction of myelination in the central nervous system by electrical activity. Proc. Natl. Acad. Sci. USA* **93,** *9887–9892 (1996).*

16. *Yamazaki, Y. et al. Modulatory effects of oligodendrocytes on the conduction velocity of action potentials along axons in the alveus of the rat hippocampal CA1 region. Neuron Glia Biol.* **3,** *325–334 (2007).*

17. *Gibson, E. M. et al. Neuronal activity promotes oligodendrogenesis and adaptive myelination in the mammalian brain. Science* **344,** *1252304 (2014).*

18. *Hines, J. H., Ravanelli, A. M., Schwindt, R., Scott, E. K. & Appel, B. Neuronal activity biases axon selection for myelination in vivo. Nat. Neurosci.* **18,** *683–689 (2015).*

19. *Mensch, S. et al. Synaptic vesicle release regulates myelin sheath number of individual oligodendrocytes in vivo. Nat. Neurosci.* **18,** *628–630 (2015).*

20. *Seidl, A. H., Rubel, E. W. & Barría, A. Differential conduction velocity regulation in ipsilateral and contralateral collaterals innervating brainstem coincidence detector neurons. J. Neurosci.* **34,** *4914–4919 (2014).*

21. *Seidl, A. H. & Rubel, E. W. Systematic and differential myelination of axon collaterals in the mammalian auditory brainstem. Glia* **64,** *487–494 (2016).*

22. *Leuzzi, V. et al. Ataxia, deafness, leukodystrophy: inherited disorder of the white matter in three related patients. Neurology* **54,** *2325–2328 (2000).*

23. *Furst, M. & Levine, R. A. Hearing disorders in multiple sclerosis. Handb Clin Neurol* **129,** *649–665 (2015).*

24. *Papakonstantinou, A., Strelcyk, O. & Dau, T. Relations between perceptual measures of temporal processing, auditory-evoked brainstem responses and speech intelligibility in noise. Hear. Res.* **280,** *30–37 (2011).*

25. *Shah, S. N. & Salamy, A. Auditory-evoked far-field potentials in myelin deficient mutant quaking mice. Neuroscience* **5,** *2321–2323 (1980).*

26. *Naito, R., Murofushi, T., Mizutani, M. & Kaga, K. Auditory brainstem responses, electrocochleograms, and cochlear microphonics in the myelin deficient mutant hamster "bt". Hear. Res.* **136,** *44–48 (1999).*

27. *Ito, T., Tokuriki, M., Shibamori, Y., Saito, T. & Nojyo, Y. Cochlear nerve demyelination causes prolongation of wave I latency in ABR of the myelin deficient (md) rat. Hear. Res.* **191,** *119–124 (2004).*

28. *Kim, J. H., Renden, R. & von Gersdorff, H. Dysmyelination of auditory afferent axons increases the jitter of action potential timing during high-frequency firing. J. Neurosci.* **33,** *9402–9407 (2013).*

29. *Roncagliolo, M., Benítez, J. & Eguibar, J. R. Progressive deterioration of central components of auditory brainstem responses during postnatal development of the myelin mutant taiep rat. Audiol Neurootol* **5,** *267–275 (2000).*

30. *Carpinelli, M. R. et al. A new mouse model of Canavan leukodystrophy displays hearing impairment due to central nervous system dysmyelination. Dis. Model. Mech. (2014). doi:10.1242/dmm.014605*

31. *Kanzaki, J., Mikoshiba, K. & Tsukada, Y. Auditory brain stem response in neuropathological mutant mice (shiverer and reeler). ORL. J. Otorhinolaryngol. Relat. Spec.* **47,** *294–298 (1985).*

846   32.   Roach, A., Boylan, K., Horvath, S., Prusiner, S. B. & Hood, L. E. Characterization of cloned cDNA
847   representing rat myelin basic protein: absence of expression in brain of shiverer mutant mice. Cell
848   **34,** 799–806 (1983).

849   33.   Boggs, J. M. Myelin basic protein: a multifunctional protein. Cell Mol. Life Sci. **63,** 1945–1961
850   (2006).

851   34.   Nawaz, S. et al. Actin filament turnover drives leading edge growth during myelin sheath formation
852   in the central nervous system. Dev. Cell **34,** 139–151 (2015).

853   35.   Rosenbluth, J. Central myelin in the mouse mutant shiverer. J. Comp. Neurol. **194,** 639–648
854   (1980).

855   36.   Poggi, G. et al. Cortical network dysfunction caused by a subtle defect of myelination. Glia **64,**
856   2025–2040 (2016).

857   37.   Readhead, C. et al. Expression of a myelin basic protein gene in transgenic shiverer mice:
858   correction of the dysmyelinating phenotype. Cell **48,** 703–712 (1987).

859   38.   Shine, H. D., Readhead, C., Popko, B., Hood, L. & Sidman, R. L. Morphometric analysis of normal,
860   mutant, and transgenic CNS: correlation of myelin basic protein expression to myelinogenesis. J.
861   Neurochem. **58,** 342–349 (1992).

862   39.   Miller, D. J., Lackey, E. P., Hackett, T. A. & Kaas, J. H. Development of myelination and cholinergic
863   innervation in the central auditory system of a prosimian primate (Otolemur garnetti). J. Comp.
864   Neurol. **521,** 3804–3816 (2013).

865   40.   Wang, J. et al. Myelination of the postnatal mouse cochlear nerve at the peripheral-central nervous
866   system transitional zone. Front. Pediatr. **1,** 43 (2013).

867   41.   Bakay, W. M. H., Anderson, L. A., Garcia-Lazaro, J. A., McAlpine, D. & Schaette, R. Hidden
868   hearing loss selectively impairs neural adaptation to loud sound environments. Nat. Commun. **9,**
869   4298 (2018).

870   42.   Buran, B. N. et al. Onset coding is degraded in auditory nerve fibers from mutant mice lacking
871   synaptic ribbons. J. Neurosci. **30,** 7587–7597 (2010).

872   43.   Moser, T. & Starr, A. Auditory neuropathy--neural and synaptic mechanisms. Nat. Rev. Neurol. **12,**
873   135–149 (2016).

874   44.   Sergeyenko, Y., Lall, K., Liberman, M. C. & Kujawa, S. G. Age-related cochlear synaptopathy: an
875   early-onset contributor to auditory functional decline. J. Neurosci. **33,** 13686–13694 (2013).

876   45.   Strenzke, N. et al. Hair cell synaptic dysfunction, auditory fatigue and thermal sensitivity in otoferlin
877   Ile515Thr mutants. EMBO J. **35,** 2519–2535 (2016).

878   46.   Wan, G. & Corfas, G. Transient auditory nerve demyelination as a new mechanism for hidden
879   hearing loss. Nat. Commun. **8,** 14487 (2017).

880   47.   Hamada, M. S. & Kole, M. H. P. Myelin loss and axonal ion channel adaptations associated with
881   gray matter neuronal hyperexcitability. J. Neurosci. **35,** 7272–7286 (2015).

882   48.   Kuba, H., Oichi, Y. & Ohmori, H. Presynaptic activity regulates Na(+) channel distribution at the
883   axon initial segment. Nature **465,** 1075–1078 (2010).

884   49.   Susuki, K. & Kuba, H. Activity-dependent regulation of excitable axonal domains. J Physiol Sci **66,**
885   99–104 (2016).

886   50.   Wu, G. K., Arbuckle, R., Liu, B.-H., Tao, H. W. & Zhang, L. I. Lateral sharpening of cortical
887   frequency tuning by approximately balanced inhibition. Neuron **58,** 132–143 (2008).

888   51.   Khouri, L. & Nelken, I. Detecting the unexpected. Curr. Opin. Neurobiol. **35,** 142–147 (2015).

889   52.   Ayala, Y. A. & Malmierca, M. S. Stimulus-specific adaptation and deviance detection in the inferior
890   colliculus. Front. Neural Circuits **6,** 89 (2012).

891   53.   Pérez-González, D. & Malmierca, M. S. Adaptation in the auditory system: an overview. Front
892   Integr Neurosci **8,** 19 (2014).

893   54.   Anderson, L. A. & Linden, J. F. Mind the gap: two dissociable mechanisms of temporal processing
894   in the auditory system. J. Neurosci. **36,** 1977–1995 (2016).

895   55.   Harris, K. C., Wilson, S., Eckert, M. A. & Dubno, J. R. Human evoked cortical activity to silent gaps
896   in noise:' ' effects of age, attention, and cortical processing speed. Ear Hear. **33,** 330–339 (2012).

897   56.   Fournier, P. & Hébert, S. Gap detection deficits in humans with tinnitus as assessed with the
898   acoustic startle paradigm: does tinnitus fill in the gap? Hear. Res. **295,** 16–23 (2013).

899   57.   Joris, P. X., Schreiner, C. E. & Rees, A. Neural processing of amplitude-modulated sounds.
900   Physiol. Rev. **84,** 541–577 (2004).

901   58.   Sinha, K., Karimi-Abdolrezaee, S., Velumian, A. A. & Fehlings, M. G. Functional changes in
902   genetically dysmyelinated spinal cord axons of shiverer mice: role of juxtaparanodal Kv1 family K+
903   channels. J. Neurophysiol. **95,** 1683–1695 (2006).

904   59.   Battefeld, A., Tran, B. T., Gavrilis, J., Cooper, E. C. & Kole, M. H. P. Heteromeric Kv7.2/7.3
905   channels differentially regulate action potential initiation and conduction in neocortical myelinated
906   axons. J. Neurosci. **34,** 3719–3732 (2014).

907   60.   Stys, P. K., Ransom, B. R. & Waxman, S. G. Compound action potential of nerve recorded by
908   suction electrode: a theoretical and experimental analysis. Brain Res. **546,** 18–32 (1991).

909   61.   Shinn, J. B., Chermak, G. D. & Musiek, F. E. GIN (Gaps-In-Noise) Performance in the Pediatric
910   Population. J Am Acad Audiol **20,** 229–238 (2009).

911   62.   Clark, M. G., Sherman, G. F., Bimonte, H. A. & Fitch, R. H. Perceptual auditory gap detection
912   deficits in male BXSB mice with cerebrocortical ectopias. Neuroreport **11,** 693–696 (2000).

913   63.   Dehmel, S., Eisinger, D. & Shore, S. E. Gap prepulse inhibition and auditory brainstem-evoked
914   potentials as objective measures for tinnitus in guinea pigs. Front. Syst. Neurosci. **6,** 42 (2012).

915   64.   Friedman, J. T., Peiffer, A. M., Clark, M. G., Benasich, A. A. & Fitch, R. H. Age and experience-
916   related improvements in gap detection in the rat. Brain Res. Dev. Brain Res. **152,** 83–91 (2004).

917   65.   Moreno-Paublete, R., Canlon, B. & Cederroth, C. R. Differential Neural Responses Underlying the
918   Inhibition of the Startle Response by Pre-Pulses or Gaps in Mice. Front. Cell Neurosci. **11,** 19
919   (2017).

920   66.   Koch, M. The neurobiology of startle. Prog. Neurobiol. **59,** 107–128 (1999).

921   67.   Popelář, J. et al. The absence of brain-specific link protein Bral2 in perineuronal nets hampers
922   auditory temporal resolution and neural adaptation in mice. Physiol. Res. **66,** 867–880 (2017).

923   68.   Walton, J. P., Frisina, R. D., Ison, J. R. & O'Neill, W. E. Neural correlates of behavioral gap
924   detection in the inferior colliculus of the young CBA mouse. J. Comp. Physiol. A **181,** 161–176
925   (1997).

926   69.   de Hoz, L. & Nelken, I. Frequency tuning in the behaving mouse: different bandwidths for
927   discrimination and generalization. PLoS One **9,** e91676 (2014).

928   70.   de Hoz, L. et al. Blocking c-Fos Expression Reveals the Role of Auditory Cortex Plasticity in Sound
929   Frequency Discrimination Learning. Cereb. Cortex **28,** 1645–1655 (2018).

930   71.   Brzózka, M. M., Rossner, M. J. & de Hoz, L. Tcf4 transgenic female mice display delayed
931   adaptation in an auditory latent inhibition paradigm. Eur Arch Psychiatry Clin Neurosci **266,** 505–
932   512 (2016).

933   72.   Cruces-Solís, H. et al. Auditory midbrain coding of statistical learning that results from
934   discontinuous sensory stimulation. PLoS Biol. **16,** e2005114 (2018).

935   73.   Chen, C., Krueger-Burg, D. & de Hoz, L. Wide sensory filters underlie performance in memory-
936   based discriminationand generalization. PLoS One (2019).

937   74.   Clarkson, C., Antunes, F. M. & Rubio, M. E. Conductive Hearing Loss Has Long-Lasting Structural
938   and Molecular Effects on Presynaptic and Postsynaptic Structures of Auditory Nerve Synapses in
939   the Cochlear Nucleus. J. Neurosci. **36,** 10214–10227 (2016).

940   75.   Lasiene, J., Matsui, A., Sawa, Y., Wong, F. & Horner, P. J. Age-related myelin dynamics revealed
941   by increased oligodendrogenesis and short internodes. Aging Cell **8,** 201–213 (2009).

942   76.   Sinclair, J. L. et al. Sound-Evoked Activity Influences Myelination of Brainstem Axons in the
943   Trapezoid Body. J. Neurosci. **37,** 8239–8255 (2017).

944   77.   Xing, Y. et al. Age-related changes of myelin basic protein in mouse and human auditory nerve.
945   PLoS One **7,** e34500 (2012).

946   78.   Chiappa, K. H., Harrison, J. L., Brooks, E. B. & Young, R. R. Brainstem auditory evoked responses
947   in 200 patients with multiple sclerosis. Ann. Neurol. **7,** 135–143 (1980).

948   79.   Amaral, M. I. R. do & Colella-Santos, M. F. Temporal resolution: performance of school-aged
949   children in the GIN - Gaps-in-noise test. Braz J Otorhinolaryngol **76,** 745–752 (2010).

950   80.   Delgutte, B. & Kiang, N. Y. S. Speech coding in the auditory nerve: IV. Sounds with consonant-like
951   dynamic characteristics. J. Acoust. Soc. Am. **75,** 897–907 (1984).

952   81.   Sinex, D. G., McDonald, L. P. & Mott, J. B. Neural correlates of nonmonotonic temporal acuity for
953   voice onset time. J. Acoust. Soc. Am. **90,** 2441–2449 (1991).

82. Noebels, J. L., Marcom, P. K. & Jalilian-Tehrani, M. H. Sodium channel density in hypomyelinated brain increased by myelin basic protein gene deletion. Nature **352,** 431–434 (1991).

83. Westenbroek, R. E., Noebels, J. L. & Catterall, W. A. Elevated expression of type II Na+ channels in hypomyelinated axons of shiverer mouse brain. J. Neurosci. **12,** 2259–2267 (1992).

84. Boiko, T. et al. Compact myelin dictates the differential targeting of two sodium channel isoforms in the same axon. Neuron **30,** 91–104 (2001).

85. Van Wart, A. & Matthews, G. Expression of sodium channels Nav1.2 and Nav1.6 during postnatal development of the retina. Neurosci. Lett. **403,** 315–317 (2006).

86. Van Wart, A. & Matthews, G. Impaired firing and cell-specific compensation in neurons lacking nav1.6 sodium channels. J. Neurosci. **26,** 7172–7180 (2006).

87. Rasband, M. N., Trimmer, J. S., Peles, E., Levinson, S. R. & Shrager, P. K+ channel distribution and clustering in developing and hypomyelinated axons of the optic nerve. J Neurocytol **28,** 319–331 (1999).

88. Wang, H., Allen, M. L., Grigg, J. J., Noebels, J. L. & Tempel, B. L. Hypomyelination alters K+ channel expression in mouse mutants shiverer and Trembler. Neuron **15,** 1337–1347 (1995).

89. Stathopoulos, P., Alexopoulos, H. & Dalakas, M. C. Autoimmune antigenic targets at the node of Ranvier in demyelinating disorders. Nat. Rev. Neurol. **11,** 143–156 (2015).

90. Battefeld, A., Klooster, J. & Kole, M. H. P. Myelinating satellite oligodendrocytes are integrated in a glial syncytium constraining neuronal high-frequency activity. Nat. Commun. **7,** 11298 (2016).

91. Jensen, H. B., Ravnborg, M., Dalgas, U. & Stenager, E. 4-Aminopyridine for symptomatic treatment of multiple sclerosis: a systematic review. Ther Adv Neurol Disord **7,** 97–113 (2014).

92. Trapp, B. D. & Stys, P. K. Virtual hypoxia and chronic necrosis of demyelinated axons in multiple sclerosis. Lancet Neurol. **8,** 280–291 (2009).

93. Shailer, M. J. & Moore, B. C. Gap detection as a function of frequency, bandwidth, and level. J. Acoust. Soc. Am. **74,** 467–473 (1983).

94. Leitner, D. S. et al. Parameters affecting gap detection in the rat. Percept. Psychophys. **54,** 395–405 (1993).

95. Weible, A. P., Liu, C., Niell, C. M. & Wehr, M. Auditory cortex is required for fear potentiation of gap detection. J. Neurosci. **34,** 15437–15445 (2014).

96. Weible, A. P. et al. Perceptual gap detection is mediated by gap termination responses in auditory cortex. Curr. Biol. **24,** 1447–1455 (2014).

97. Hoover, E., Pasquesi, L. & Souza, P. Comparison of clinical and traditional gap detection tests. J Am Acad Audiol **26,** 540–546 (2015).

98. Phillips, D. P. Auditory gap detection, perceptual channels, and temporal resolution in speech perception. J Am Acad Audiol **10,** 343–354 (1999).

989 99.   Moshitch, D., Las, L., Ulanovsky, N., Bar-Yosef, O. & Nelken, I. Responses of neurons in primary
990   auditory cortex (A1) to pure tones in the halothane-anesthetized cat. J. Neurophysiol. **95,** 3756–
991   3769 (2006).

992 100. Monje, M. Myelin plasticity and nervous system function. Annu. Rev. Neurosci. **41,** 61–76 (2018).

993 101. Werner, H. B. et al. A critical role for the cholesterol-associated proteolipids PLP and M6B in
994   myelination of the central nervous system. Glia **61,** 567–586 (2013).

995 102. Jung, S. et al. Disruption of adaptor protein 2μ (AP-2μ) in cochlear hair cells impairs vesicle
996   reloading of synaptic release sites and hearing. EMBO J. **34,** 2686–2702 (2015).

997 103. Weil, M.-T., Ruhwedel, T., Meschkat, M., Sadowski, B. & Möbius, W. Transmission electron
998   microscopy of oligodendrocytes and myelin. Methods Mol. Biol. **1936,** 343–375 (2019).

999 104. Hackett, T. A., Barkat, T. R., O'Brien, B. M. J., Hensch, T. K. & Polley, D. B. Linking topography to
1000   tonotopy in the mouse auditory thalamocortical circuit. J. Neurosci. **31,** 2983–2995 (2011).

1001 105. Ashida, G., Wagner, H. & Carr, C. E. in Analysis of parallel spike trains (eds. Grün, S. & Rotter, S.)
1002   59–74 (Springer US, 2010). doi:10.1007/978-1-4419-5675-0_4

1003

Figure 1
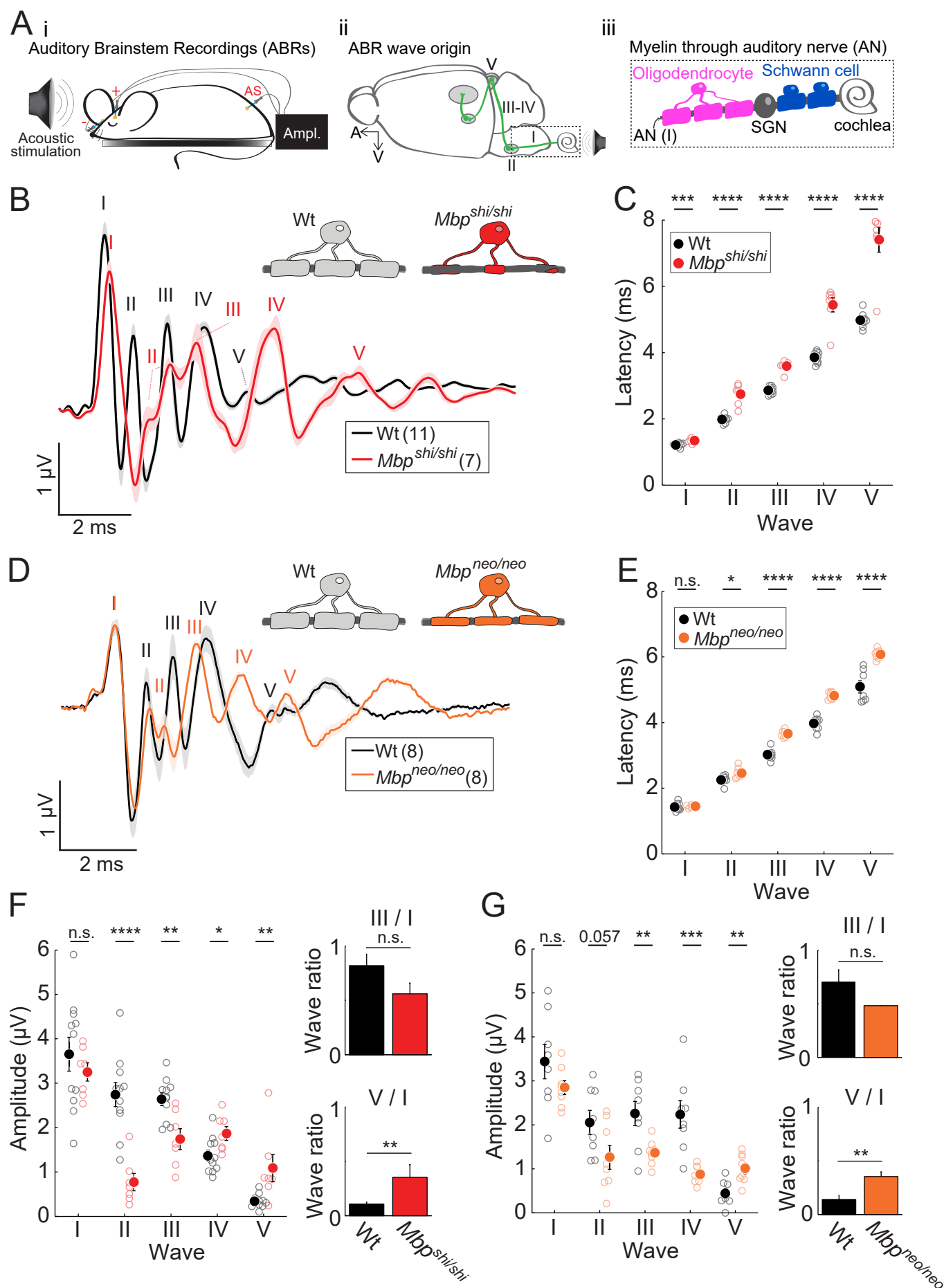
Figure 1. Central dysmyelination causes evoked-response delays and gain changes.

A) Left (i): Schematic of auditory brainstem (ABR) scalp recordings in mice. Middle (ii): structures in the auditory circuit contributing to ABRs (I to V). Right (iii): scheme of peripheral (around the spiral ganglion neurons, SGN) and central myelination of auditory nerve (AN). **B)** Group mean traces in control (black; n=11; 7 $Mbp^{+/+}$ and 4 $Mbp^{shi/+}$ without significant differences in ABR measurements (80 dB), see table in Figure S2D) and $Mbp^{shi/shi}$ (red; n=7) mice. Each one of the 5 peaks (I–V) can be attributed to activity at a different station along the auditory brainstem (see schematic in Aii). Responses in $Mbp^{shi/shi}$ mice were delayed at all auditory stations. Wave II appears divided and merged with wave III. **C)** The quantification of the peak latencies reveals a progressively larger difference in latency from wave I (p=0.001) to wave V (p<0.0001 for waves II-V). **D)** Same as A) but for $Mbp^{neo/neo}$ mice (orange; n = 8) and Wt (black; n=8). Wave II appears divided. **E)** Latency quantification again showed progressively larger latency differences from wave I to wave V (p=0.74, p=0.013, p<0.0001, p<0.0001, p=0.0001; waves I-V, respectively). **F)** Wave amplitude quantification. In $Mbp^{shi/shi}$ mice (red), waves II and III amplitudes were reduced, while those of waves IV and V were increased (p=0.44, p<0.0001, p=0.0031, p=0.022, p=0.008; waves I to V respectively), suggesting a compensatory central gain increase. Auditory gain was quantified by the amplitude ratio in waves III/I (upper right graph), which was comparable across groups (p=0.085), and waves V/I (lower right graph), which was significantly increased in mutants (p=0.006). **G)** Same as E but for $Mbp^{neo/neo}$ mice. As in $Mbp^{shi/shi}$ mice, amplitude changes were seen at the central level (p=0.18, p=0.057, p=0.009, p=0.0008, p=0.003; waves I to V respectively). An increase in central gain was observed in $Mbp^{neo/neo}$ for wave V (lower right graph; p=0.009) but no changes in the gain of wave III (upper right graph; p=0.083). All graphs depict the mean and S.E.M. (error bar or a shaded area).

Figure 2

A — Inferior colliculus (IC)



B — Layer IV auditory cortex (ACx)
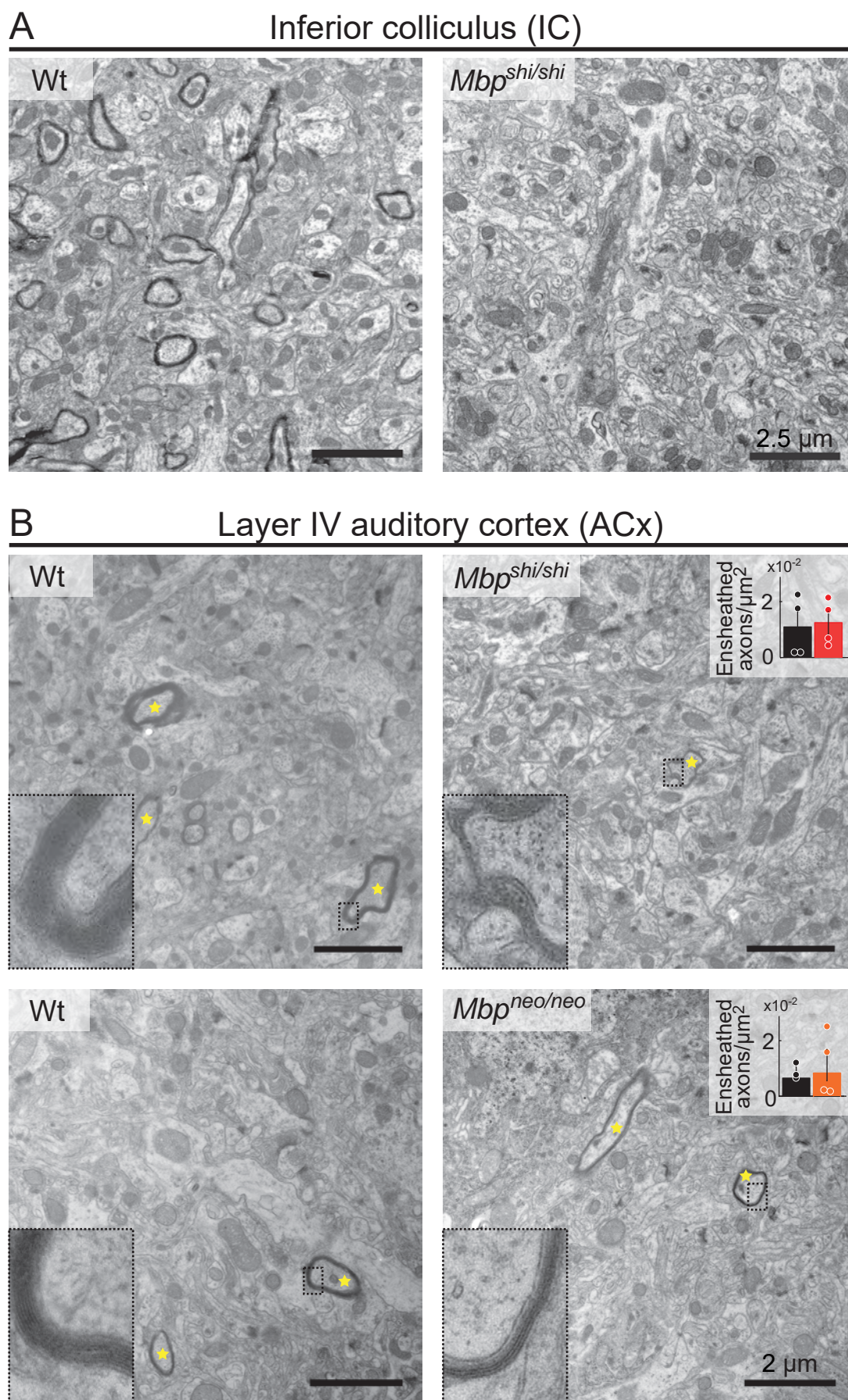
Figure 2. Ensheathment profiles along the auditory system in normal and dysmyelinated models.

A) Electron microscopy images of the inferior colliculus of a Wt mouse (left panel) showing sparse compact myelin, and an *Mbp*^{shi/shi} mouse (right panel), lacking electro-dense compact myelin. **B)** Electron microscopy images of the auditory cortex of Wt and *Mbp*^{shi/shi} (upper panel) and Wt and *Mbp*^{neo/neo} mouse (lower panel). Ensheathed axons in the ACx are marked with yellow asterisks. Insets show details of the myelin sheath of axons from the respective image. *Mbp*^{shi/shi} axons (upper right) show lack of compact myelin, while *Mbp*^{neo/neo} axons (lower right) show thinner compact myelin than Wts. Inset plots show the quantification of the number of ensheathed axons (compact or not compact myelin) per area in *Mbp*^{shi/shi} (left, red, n=4), *Mbp*^{neo/neo} (right, orange, n=4), and their respective Wts (black, n=3-4). There was no difference between Wt and either mutant model (p=0.83 and p=0.73 for *Mbp*^{shi/shi} and *Mbp*^{neo/neo} respectively). Bar graphs show the mean of all animals quantified (10-15 images per mouse). Scale bars: 2.5 µm (A), 2 µm (B).
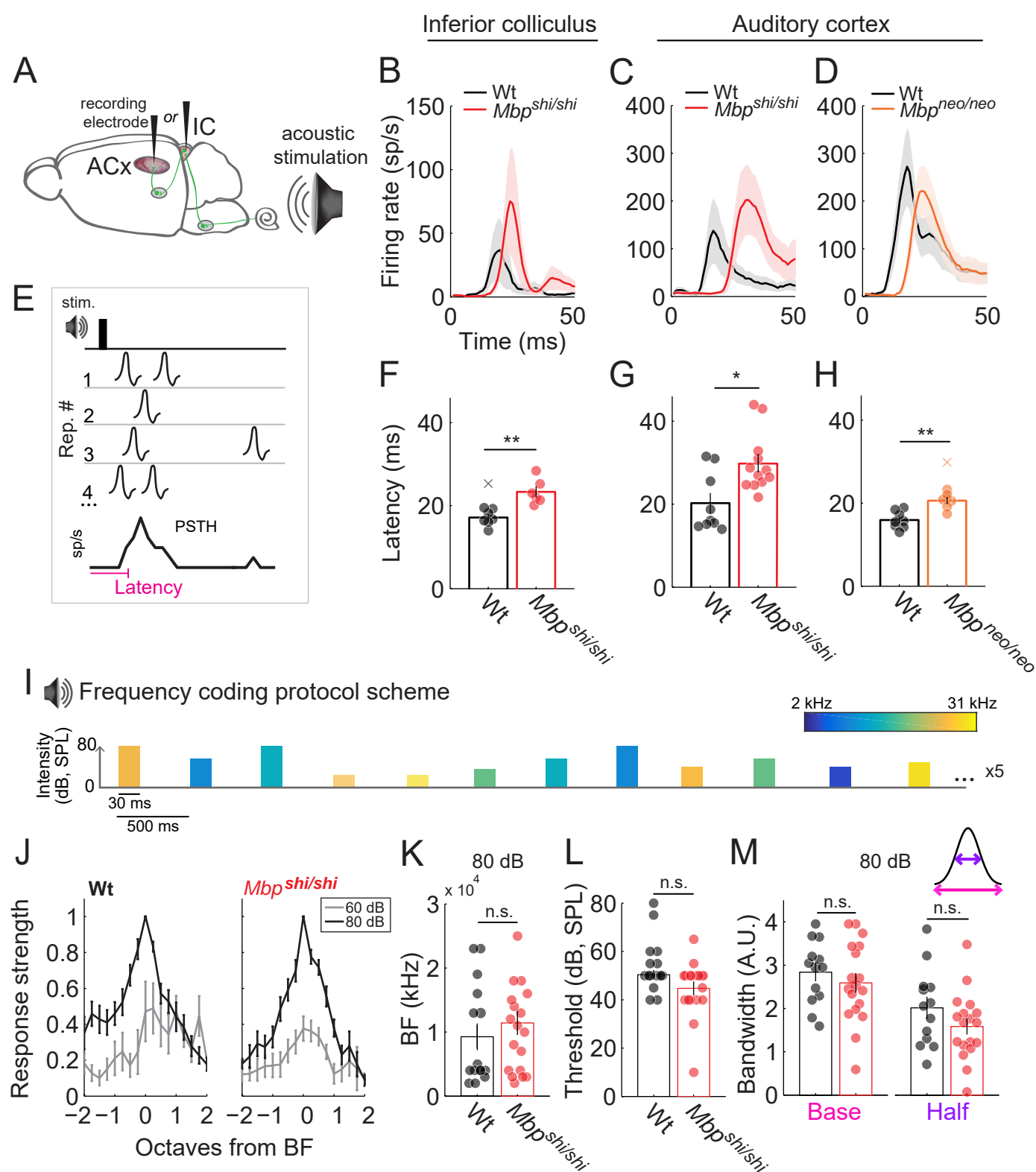
Figure 3

Figure 3. Responses to single sound-stimuli in IC and ACx of dysmyelinated models are abnormal only in latency.

A) Schematic brain depicting auditory areas (ACx and IC) where multi-unit recordings took place. **B)** Peri-stimulus time histogram (PSTH) of responses to a click sound recorded in the IC for Wt (black; n=6-8) and *Mbp$^{shi/shi}$* (red; n=6-8) mice aligned at time of click presentation (0 ms). Responses of *Mbp$^{shi/shi}$* are delayed with respect to Wt. **C)** Same as B) but for ACx recordings. A stronger delay in *Mbp$^{shi/shi}$* (red; n=12-13) compared to Wt (black; n=7-10) is observed in this case. **D)** Same as C) but for *Mbp$^{neo/neo}$* mice (orange; n=7-8) and corresponding Wt (black; n=8). A smaller shift in latency in the ACx of *Mbp$^{neo/neo}$* is observed, compared to *Mbp$^{shi/shi}$* mice. **E)** Scheme of latency measurement: time at which the PSTH, sum of spikes across 10 trials in 1 ms time windows, surpassed 1.5 times the baseline activity. A significant latency increase is seen in *Mbp$^{shi/shi}$* animals compared to Wt. **F)** in the IC (p=0.0012) and **G)** in the ACx (p=0.023). **H)** *Mbp$^{neo/neo}$* mice also showed a significant increase in response latency in the ACx (p=0.0012). **I)** Schematic of the tone sweep protocol used to test tuning. A series of 24, 30 ms long, tones (2-31 kHz) were played at different intensities. 10 repetitions (Rep.) of each tone-intensity combination were presented in a random order. **J-M)** Basic tuning properties are not affected with dysmyelination. n=13 recordings of 10 wild type mice. n=18 recordings of 15 *Mbp$^{shi/shi}$* mice. **J)** Normalized tuning curves for wild type (left) and *Mbp$^{shi/shi}$* mice show response selectivity in octaves from best frequency (BF) at 60 (gray) and 80 dB (black). **K)** Recordings from comparable rostro-caudal locations yielded comparable BFs at 80 dB (p=0.51) in wild type and *Mbp$^{shi/shi}$* mice indicating no major change in tonotopic map. **L)** Auditory cortical thresholds were similar between groups (p=0.11). **M)** Bandwidth of tuning was also similar between groups (p=0.56 and p=0.21 for base and half bandwidth respectively).

Figure 4

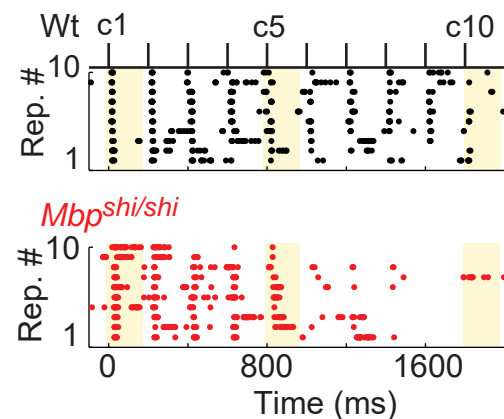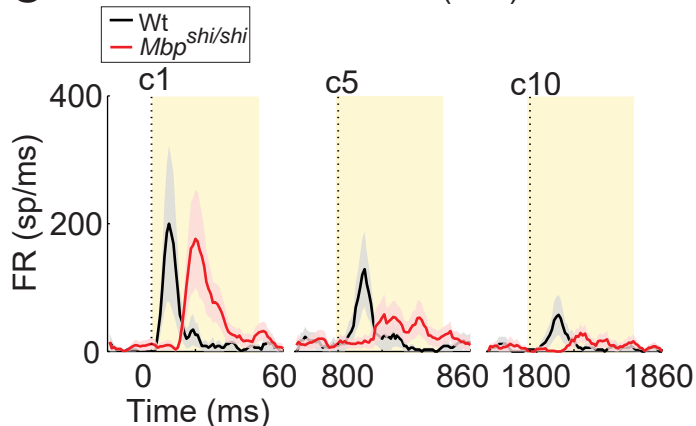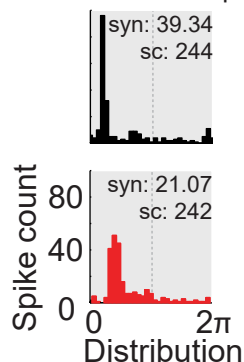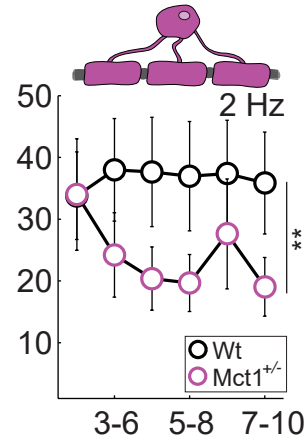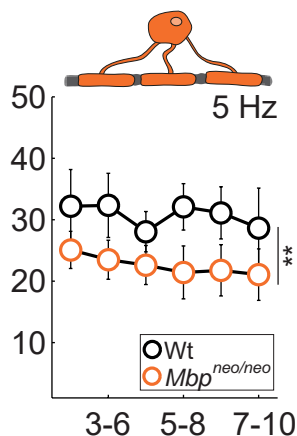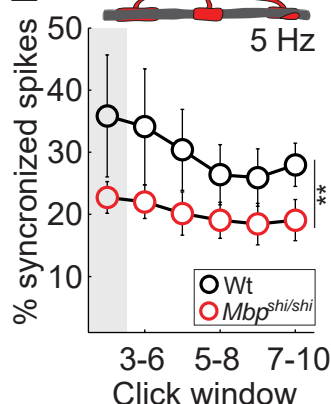**Figure 4. Temporal reliability is affected in mice with either dysmyelination or a reduction in axo-glial metabolic support.**

A) Schematic of the click rate-tracing protocol used to test temporal reliability. Blocks of 10 clicks are played at different rates in random order. Each rate is repeated 10 times. Analysis in C) focuses on click 1, 5 and 10 (c1, c5 and c10). **B)** Example raster plot of ACx responses (each dot represents 1 spike) to 10 clicks at 5 Hz across the 10 stimulus repetitions in a Wt (upper, black) and an $Mbp^{shi/shi}$ mouse (lower, red). $Mbp^{shi/shi}$ animals show a steeper decay on spiking activity across clicks compared to Wt. **C)** Mean PSTH of responses to click 1, 5 and 10, at 5 Hz for Wt (black; n=10) and $Mbp^{shi/shi}$ (red; n=13) animals. The thick line shows the mean of all recorded animals and the shaded area depicts the S.E.M. Click time is indicated by dashed lines. While responses to the first click are similar in amplitude in Wt and $Mbp^{shi/shi}$ animals (with the expected delay in $Mbp^{shi/shi}$), a strong reduction of response strength is seen in $Mbp^{shi/shi}$ mice with increasing clicks. **D)** Individual examples of spike synchrony plots for Wt (top) and $Mbp^{shi/shi}$ (bottom) were taken from the first click window (clicks 2-5, depicted by a gray square in E). **E)** Quantification of spike synchrony in sliding windows of 4 clicks (clicks 2-5, 3-6, 4-7, 5-8, 6-9 and 7-10). Onset responses of click 1 were not used. Leftmost: significant reduction in spike synchrony between $Mbp^{shi/shi}$ mice (red, n=6-9) and Wt (black, n= 3-6 mice) at 5 Hz (p=0.0021). Middle: significant reduction also seen between $Mbp^{neo/neo}$ mice (orange, n=5-8 mice), and Wt (black, n=3-8 mice) at 5 Hz (p=0.0014). Right: significant difference between MCT1$^{+/-}$ mice (purple, n=5-6 mice), and Wt (black, n=8 mice) at 2 Hz (p=0.011).
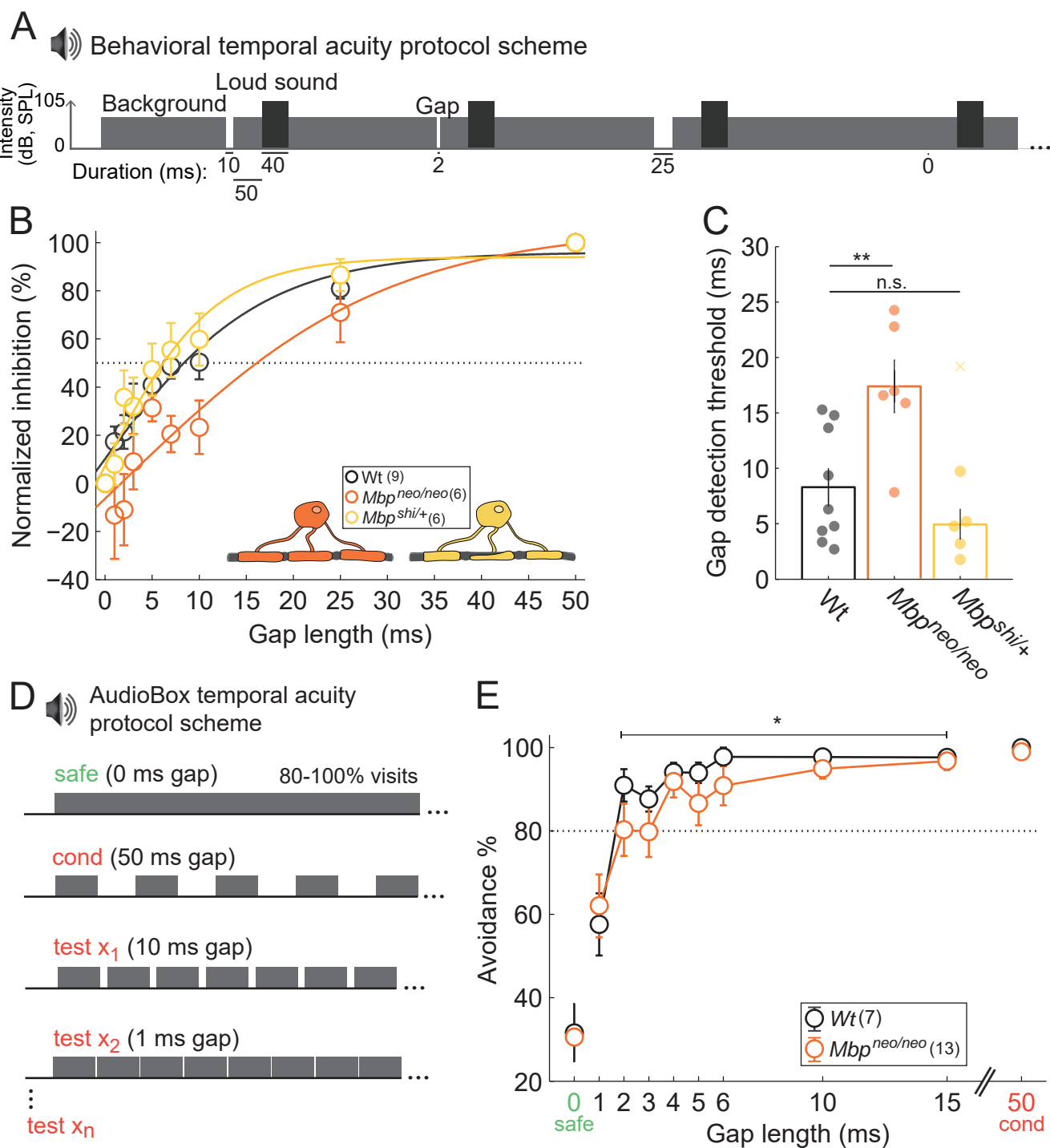
Figure 5
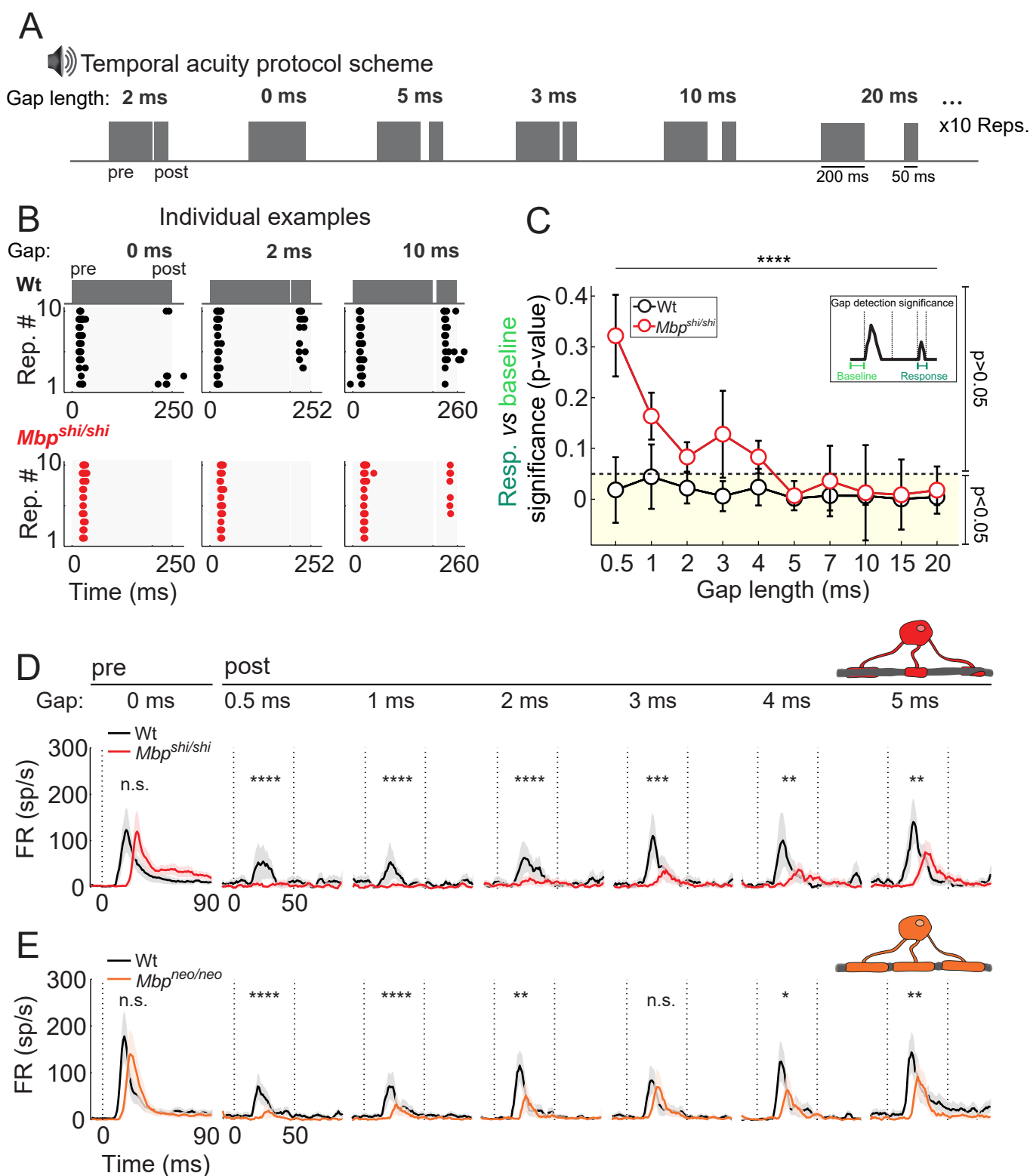
Figure 5. Cortical temporal acuity is impaired with CNS dysmyelination.

A) Schematic of the gap-detection protocol used to test temporal acuity. A 200 ms long broad-band noise (BBN) pulse (pre) was followed by a silent gap and a second 50ms long BBN pulse (post). Gap lengths ranged from 0-50 ms. Each pre-gap-post sequence was repeated 10 times for every gap length. **B)** Individual example of ACx spikes (dots) evoked during sound presentation (gray patches) and gaps of 0 ms (left), 2 ms (center), and 10 ms (right) length in a Wt (upper, black) and a *Mbp*^{shi/shi} (lower, red) mouse during 10 stimulus repetitions (y axis) per gap length. **C)** Quantification of gap-detection significance (median statistical difference (p-value) between the baseline and the post-gap response per recording; see diagram above). A significant effect of gap-length between groups ($p<0.0001$), demonstrates that the gap detection rate in *Mbp*^{shi/shi} (n=14-20 recordings from 14 mice) is lower than for Wt (n=12-15 recordings from 12 animals) for the shorter gaps. Error bars: standard error of the median. Dotted line: threshold at 0.05. Yellow shadow: significant gap-detection. **D)** Average PSTH across animals for Wt (black; n=12) and *Mbp*^{shi/shi} (red; n=14) with S.E.M. as shaded area. Left to right: pre-gap responses followed by post-gap responses for 0.5 to 5 ms gaps. Significant effect of group was seen for all post-gap responses but not for pre-gap responses ($p=0.46$, $p<0.0001$, $p<0.0001$, $p<0.0001$, $p=0.0002$, $p=0.0014$, $p=0.006$; pre-gap and 0.5 to 5 ms post-gap respectively). **E)** Same as in D) but for *Mbp*^{neo/neo} (orange; n=8) mice and their respective Wt (black; n=7). Significant effect of group was seen for most post-gap responses but not for pre-gap responses ($p=0.60$, $p<0.0001$, $p<0.0001$, $p=0.0015$, $p=0.19$, $p=0.01$, $p=0.003$; pre-gap and 0.5 to 5 ms post-gap respectively). In D) and E), dotted vertical lines at time 0 ms depict the start of the sound, and at time 50 ms the end of the post BBN.
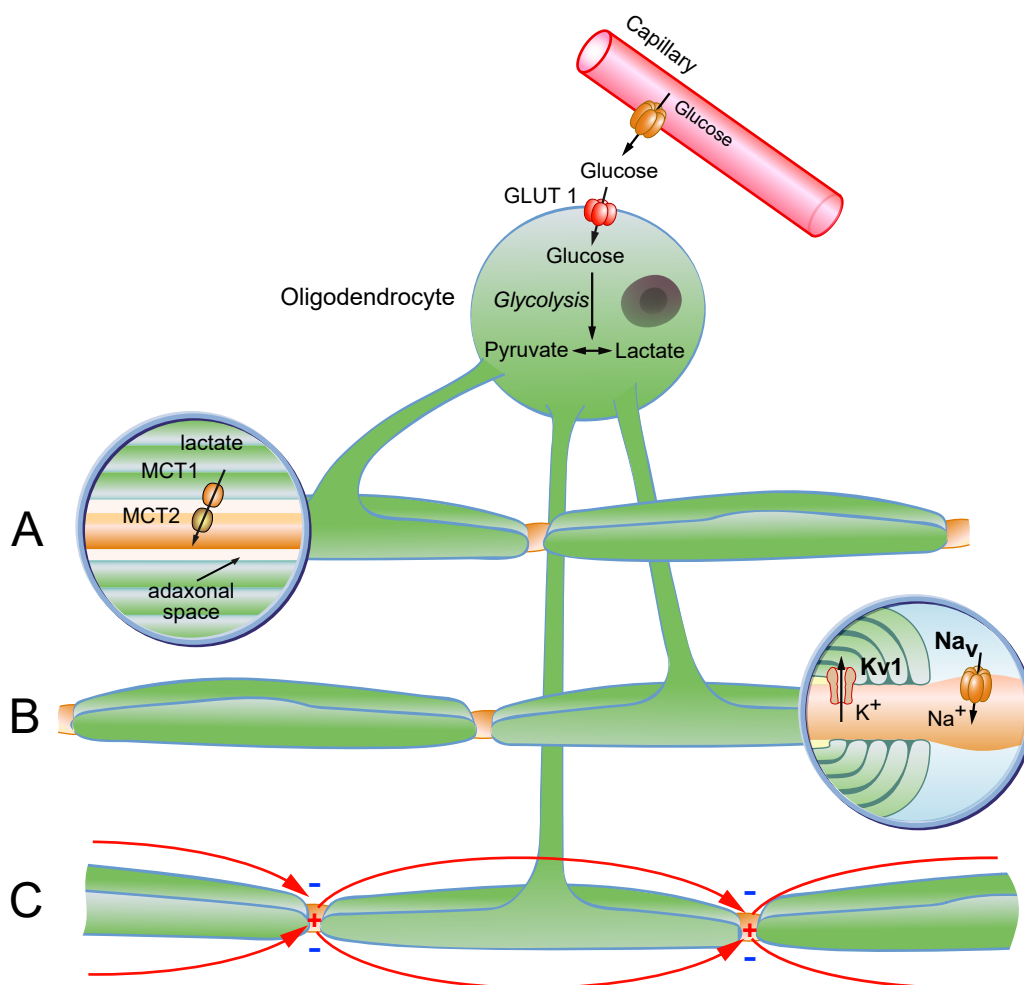
Figure 6

A 🔊 Behavioral temporal acuity protocol scheme

B

C

D 🔊 AudioBox temporal acuity protocol scheme

E

Figure 6. Behavioral temporal acuity is impaired by CNS dysmyelination.

A) Schematic of the auditory startle reflex (ASR) sound protocol. Constant background broad-band noise (BBN; 70 dB) interrupted by a startle noise at random times (105 dB; 40 ms), occasionally preceded by a silent gap of varying length. All gaps presented were followed by 50 ms background sound before the startle appearance. Each gap-startle combination was repeated 10 times. **B)** The percentage of ASR inhibition elicited by the different gaps showed a strong relationship between the gap length and the startle inhibition. $Mbp^{neo/neo}$ but not $Mbp^{shi/+}$ mice (with a 50% reduction in Mbp) showed impaired inhibition of the ASR. Dotted line: threshold at 50% inhibition used for statistical analysis in C. **C)** Gap detection threshold is increased in $Mbp^{neo/neo}$ mice (p=0.0048), but not $Mbp^{shi/+}$ (p=0.36; outlier depicted with a cross), compared to Wt animals. **D)** Schematic of sounds used in the Audiobox paradigm. Safe visits to corner were accompanied by the safe sound (0 ms gap embedded in continuous BBN, ~70 dB), and water was available. Conditioned visits were accompanied by the conditioned sound (cond; BBN with 50 ms gaps) water was not available and air-puff was delivered upon nose-poke. Once animals discriminated safe and conditioned, test visits with test sounds (gaps > 0 ms and <50 ms) were introduced. Water was available in these visits. **E)** Quantification of avoidance behavior (proportion of visits without nose-pokes) revealed a reduction (p=0.030) in $Mbp^{neo/neo}$ animals (orange; n=13) for gaps >1 ms compared to Wt (black; n=7) confirming a behavioral deficit in temporal acuity in a naturalistic environment. All graphs show the mean per group. Error bars depict the S.E.M.

Figure 7

Figure 7. Role of oligodendrocytes in information processing extends beyond conduction velocity regulation to energy support of axons and excitability of axon initial segment and nodal.

Schematic of oligodendrocyte and compact myelin (green) wrapping around 3 axons (brown) **A)** Glycolytic oligodendrocytes can support axons via the transport of glycolytic end products, such as lactate or pyruvate. **B)** The maintenance of axonal-excitable domains through clustering of ion channels depends on myelin compaction. **C)** Myelin is essential for the formation of axonal excitable domains and contributes to the speeding up of action potential conduction.